Analyst

Accepted Manuscript

This article can be cited before page numbers have been issued, to do this please use: C. Chen and J. Wang, *Analyst*, 2020, DOI: 10.1039/C9AN01998G.

ROYAL SOCIETY OF CHEMISTRY

rsc.li/analyst

DOI: 10.1039/C9AN01998G

Optical Biosensors: an exhaustive and comprehensive review

Chen Chen* and Junsheng Wang
College of Information Science and Technology, Dalian Maritime University, Dalian, 116026, China.
Email: dlmuchen@dlmu.edu.cn*; wangjsh@dlmu.edu.cn

Abstract

Optical biosensors present good performance in detecting biological systems and promote significant advances in clinical diagnostics, drug discovery, food process control, and environmental monitoring. Without complexity in the pretreatment and probable influence on the nature of target molecules, these biosensors have extra strengths including high sensitivity, robustness, reliability and potential to be integrated in one chip. In this review, the state of the art in optical biosensor technologies, including surface plasmon resonance (SPR), optical waveguide, optical resonator, photonic crystal and optical fiber are presented. Principle in terms of each type of biosensor is introduced concisely and particular emphasis has been placed on the achievements which have been gained nowadays. The strength and weakness of each kind of biosensor have been outlined as well. Concluding remarks regarding the perspectives of further developments are discussed.

Keywords: optical biosensor, optical waveguide, surface plasmon, photonic crystal, optical fiber

1. Introduction

Biosensors are analytical devices incorporating a biological sensing element. Biosensors are capable of detecting biomolecules in a complex sample by converting the physical or chemical signal to an optical signal or electrical signal which can be further processed to the concentration of the analyte[1]. The components include sensing unit, signal transducing and processing units (**Figure 1**). Molecular recognition and interaction underlie the sensing and detecting[2]. Biomolecules, i.e. antigen/antibody, enzyme, nuclear acid, hormone receptor, live cell and tissue, specifically recognize other biological entities via catalysis and affinity binding. The former based on the nature of enzyme, i.e. specific recognition and high efficient catalysis, requires a

complete dynamic analysis which is usually accompanied by many influential factors. Unfortunately, sensors based on such mechanism with poor stability and repeatability set limits on the real application. In the affinity reaction, molecular recognition depends on affinity and specificity resulting in the formation of a stable complex. Only thermodynamic equilibrium is required to be detected and thus makes sensors based on affinity binding a bright future. The recognition from a biological entity is converted to a distinguishable electrical signal, optical signal and thermal signal by the means of transducing unit. Optical signal with high sensitivity, immunity to external disturbance, stability, and low noise takes advantages over other physical signal. Therefore, optical biosensors present good performance in detecting biological systems and promote significant advances in clinical diagnostics, drug discovery, food process control, and environmental monitoring[3]. Without complexity in the pretreatment and probable influence on the nature of target molecules, these biosensors take advantages over the traditional sensors with labels.

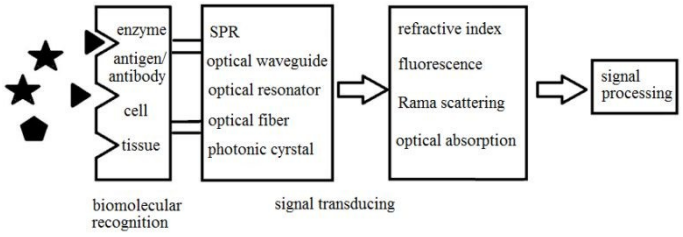

Figure 1. Graphical illustration of the component of optical biosensor. Its components include sensing unit, signal transducing and processing units.

Most optical biosensors make use of evanescent field to sense the target objects and ambient medium (**Figure 2**). Within the evanescent field, analytes recognize with partner receptors which have already been immobilized onto the surface of a waveguide and thus affected the guiding properties of the waveguide, concretely, shifts in effective mode index. The variation of the effective mode index can be assessed by the optical properties of waveguide, i.e. phase, amplitude, resonant momentum, and the variation is corresponding to the concentration of the object and the biomolecular conformation[4]. For most waveguide systems, the evanescent wave decays exponentially with decay length in the order of 0.1-1μm, thus preventing the unspecific binding event and making the evanescent-based biosensors the most promising techniques for the detection of

targets in complex real samples. The effective mode index changes can be induced by two different effects as follows[5]:

(1) the formation of a biolayer of adsorbed molecules, which are convected or diffused from a liquid sample to the waveguide surface. The biolayer is normally deemed as a homogeneous layer with thickness a and refractive index n_l.

(2) refractive index n_s changes of liquid sample covering the waveguide surface.

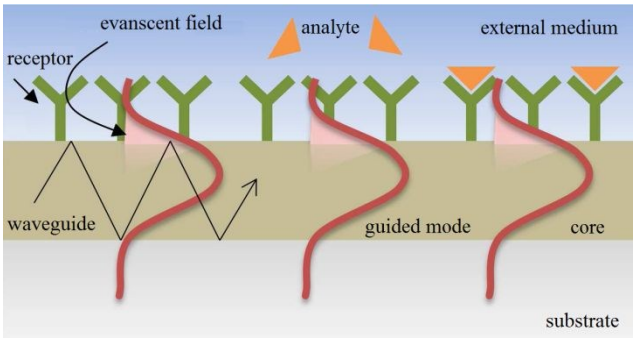

Figure 2. Scheme of the evanescent field sensing. Reproduced from ref. 4. Reproduced from ref. 4 with permission from [John Wiley &Sons.], copyright [1999-2019].

Accordingly, biosensors are applied in the bulk sensing which refers to detect any change in the bulk index of the solution covering the sensor surface and the surface sensing which involves any accumulation of mass on the sensor surface. In the sensor development, sensitivity (S) and detection limit (DL) are the important parameters to define a biosensor performance. Sensitivity which is referred to the strength of light-matter interaction is the magnitude change of transduction signal in response to the change of analyte. In most evanescent-based biosensor, it depends on the fraction of optical wave in bulk solution or the light intensity on the sensor surface. The DL is defined as the smallest detectable amount of analyte and is determined by the resolution of a read-out system. For an experimental value, it is strongly related to the noise might arising from light source intensity fluctuation, temperature fluctuations, etc. Taking into account of overall noise, the DL can be expressed as the minimum resolvable signal[6]:

$$DL = \sigma/S \quad (1)$$

where σ is the noise in the transduction signal. Although the sensitivity is high, the associated noise will cause a moderate DL value. For an optical biosensor, typically there are three ways to specify the DL. For bulk sensing, DL in a unit of refractive index unit (RIU) is used to quantify a biosensor performance. For surface sensing, surface

mass density or total mass in a unit of pg/mm^2 or pg, reflects the intrinsic sensing capability of a transducer. The third way is to use analyte concentration in a unit of in ng/mL or molarity, which is quite easy to determine as no information of the surface mass density required. This value is determined by the target molecule and its affinity constant and thus is not comparable among different sensors. These DLs in different formats are correlated and the best value for bulk index changes are within the range of 10^{-6} to 10^{-8} RIU, meaning that the sample concentration down to ng/ml or pg/ml can be determined.

Optical biosensors are easily miniaturized and present potential for chip integration. It is possible to integrate other functionalities, e.g. microfluidics, in a single platform and make a lab-on-a-chip device come true. Integrated devices are commonly in the dimension of micron and nano structure which maintain a small and elliptical mode field, whereas a standard single mode fiber has a relatively large (9-10 μm) and circular mode field. The optical mode from fiber mismatches with that in the sensor leading to the mode coupling loss of a direct butt coupling (normally in tens of dB)[7]. To improve the above scenarios, various methods are demonstrated by researchers and generally that can be classified as: the tapered coupler and the grating coupler. The tapered couplers already reported fall into three categories according to the configurations: laterally tapered waveguide, vertically tapered waveguide, and multiple tapered waveguide (**Figure. 3**). In the year of 1994, a nonlinearly tapered waveguide which has a uniform height but varying width was first used to provide very low-loss coupling with fibers (less than 0.5dB). This tapered waveguide with a taper length less than 0.7 mm had therefore a great significance for compact optoelectronics integration[8]. In the year of 2003, Day *et al.*[9] demonstrated a novel laterally tapered structure and showed a dramatic reduction of insertion loss in an optoelectronics integration (coupling loss around 0.5dB) (**Figure 3a**). The extra advantage of such configuration was that it could be implemented by a standard lithography technology[10]. Afterwards, a symmetric vertical coupler which did not achieve horizontal mode conversion was reported by Sure *et al.*[11] (**Figure 3b**). Such coupler showed a good performance on a compact monolithic integration, but complicated fabrication

involving a mask for the grayscale exposure was the main constraint on its commercialization. Fijol *et al.*[12] reported a wedge converter with a symmetric lateral taper, flat bottom and vertically tapered top surface (**Figure 3c**). The converter was comprised of the input and output ends of the tapers. The mode at the input end matched that of a standard fiber, while the output end was tuned to match the modes in different waveguide. However, fabrication of lateral and vertical stretching would pose a challenge to the current technique.

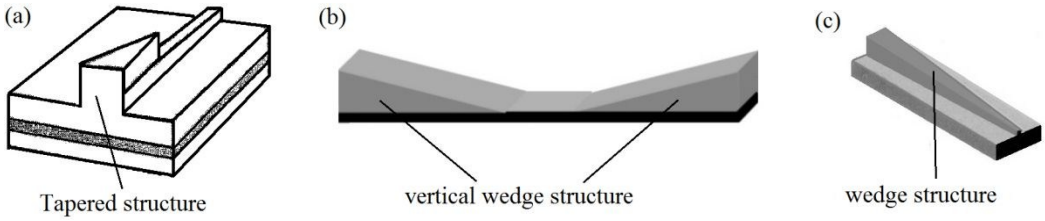

Figure 3. Three types of tapered waveguides. (a) Laterally tapered waveguide. Reproduced from ref. 9 with permission from [Optical Society of America] copyright [2003] (b) Vertically tapered waveguide. Reproduced from ref. 11 with permission from [Optical Society of America], copyright [2003] and (c) Multiple tapered waveguide. Reproduced from ref.12 with permission from [SPIE], copyright [2020].

Grating couplers without the demand of a spot-size converter allow for butt-coupling light from a fiber to a compact planar waveguide. The grating is required to provide strong coupling and large overlap between the grating and the waveguide modes. On the strength of the simplified process and on-wafer testing, grating coupler shows a great potential for development. According to the propagation direction of an incident wave, grating couplers are categorized as: vertical and parallel configurations[13]. In the early year of 2005, researchers from Ghent university[14] proposed a grating coupler with ability to efficiently couple light between a silicon-on-insulator (SOI) nanophotonic waveguide and a standard fiber (**Figure 4a**). For this coupling scheme to work, the beam entered at an angle of 8-degree, afterwards making a 90-degree turn from the fiber to the waveguide. A wedge waveguide was introduced to connect the broad waveguide of grating coupler with a narrow photonic waveguide device. To improve the coupling efficiency, a poly-silicon layer was added on top of the waveguide film prior to the formation of grating structure[15] (**Figure 4b**). The theoretical value of coupling efficiency achieved as high as 78%. Adoptions of metal

film or Bragg reflectors beneath the buried oxide did promote the ability of a conventional grating coupler, but at the expense of complicated processing[16,17]. Without a 90-degree bending of incident wave, Masanovic *et al.*[13] proposed a new structure named dual grating-assisted directional coupler which was consisted of two gratings. Incident wave was butt coupled to a thick SiON layer and subsequently to a silicon nitride (Si_3N_4) intermediate via first grating, and finally to a SOI waveguide by the second grating (**Figure 4c**). The coupling efficiency achieved 90% theoretically. However, the growth of multilayer made such configuration hard to implement.

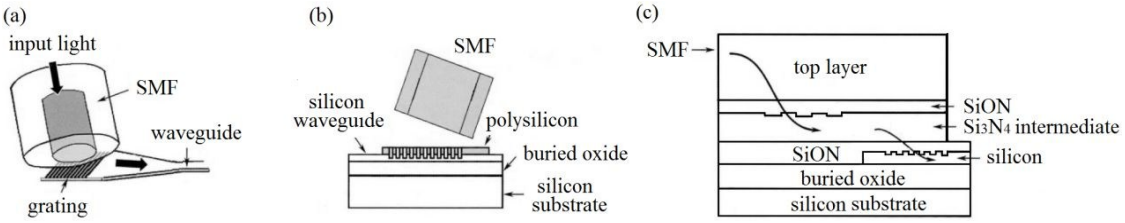

Figure 4. Different types of grating couplers. (a) An ordinary grating coupler. Reproduced from ref. 14 with permission from [IEEE], copyright [2020]. (b) Grating coupler with a poly-silicon layer. Reproduced from ref. 15 with permission from [Optical Society of America], copyright [2006]. (c) A dual grating-assisted directional coupler. Reproduced from ref. 13 with permission from [IEEE], copyright [2020].

In this review, we describe the recent advancement in optical biosensors and focus on the following configurations which represent the mainstream of research in biosensor, i.e. (1) surface plasmon resonance (SPR) based biosensor, (2) optical waveguide based biosensor, (3) optical resonator based biosensor, (3) photonic crystal based biosensor, and (4) optical fiber based biosensor. We will particularly present the work done after the year of 2015, mainly during the last two years. For each structure, a brief description of mechanism, performance and application will be illustrated. Finally, a future outlook a conclusion of the optical biosensor will be discussed.

2. Biofunctionalization strategies

Appropriate immobilization of bioreceptors on the sensor surface has played a crucial role in the detection and thus enormous efforts were went into the investigation of novel biofunctionalization strategies[18-21]. A good immobilization should make an efficient coverage of the sensor surface with bioreceptors, while keeping their nature properties, but also guarantee the stability for storage and regeneration. When it comes

to the clinical diagnosis, a well-defined surface with biomolecules is required so as to prevent a non-specific adsorption in analysis of a complex real sample. Note, that chemical activation of the sensor surface is always needed prior to the immobilization. Since silicon, silicon nitride and silica are commonly used materials, well-known silane chemistry is employed to functionalize the optical transducers[22]. The organosilanes in different structure, length, functionality and physicochemical property are nowadays on the market, amongst which the most frequently used are those with short alkyl chain, ending with amino, thiol, epoxy or carboxylic groups. Come back to the topic, the biofunctionalization strategies. Immobilization methods which have already been reported are outlined as[4]: (1) physical adsorption, (2) covalent binding, (3) physical entrapment in a hydrogel, and (4) chemical cross-linking.

Physical adsorption is determined by the hydrophobic and electrostatic interactions between the bioreceptors and the surface. The operating process is simple. However, bioreceptors are easily rinsed off in a flow condition. The nature of active receptors might be destroyed by an organic solvent or a salt solution in a high concentration and high pH when a regeneration cocktail is uploaded to the sensor. The poor adsorption of receptors and the possible damage of nature biomolecules in a regeneration process make it not desirable even though its simplicity. By the means of covalent bond, biomolecules can be immobilized on a transducer surface. The exposure of binding site of biomolecule is required so as to subsequently recognize the target molecule with high specificity and affinity. A number of chemical groups are used to form covalent bonds. Amino, carboxylic or thiol groups are preferred to couple protein molecules. It is possible to incorporate a chemical group at the end of DNA sequence benefiting from the versatility of the nuclear acid synthesis. Antibodies/antigens should be attached in an oriented way so as to leave the binding sites free, which can be fulfilled by affinity proteins, e.g. A or G protein[23]. Alternatively, bioreceptors can be physically entrapped in hydrogel. The preferable hydrogel is sol-gel, a glassy silica generated by polymerization of silicate monomers in the presence of the biological element[24,25]. The features of hydrogel, in terms of stability, wearability and strength make it attractive material used in the development of biosensor. By the use of bifunctional agents,

biomolecules can be immobilized on the sensor surface as well[26-29]. The agents, e.g. glutaraldehyde, toluene diisocyanate, diazobiphenyl, are tightly and directly bond with bioreceptors. But the complex process associating with the possible destruction of the native molecule hinders its application and development. All in all, a desirable immobilization strategy is a significant issue to achieve a full potential of an optical biosensor.

3. Optical biosensors

Up to date, researchers have invested a lot of efforts in the field of biosensing and already made a variety of configurations. Herein, we will elaborate on the description of different types of optical biosensors in terms of their working principles, features and properties, and prospects.

3.1 Surface plasmon resonance based biosensors

SPR is currently the most widespread and well-known technology, which detects the shift in refractive index caused by molecular interaction at a metal surface via surface plasmon wave[30]. Surface plasmon occurs when photons from incident wave interact with electrons in the metal surface. The plasmon propagates parallel along the metal surface thereby forming a surface plasmon wave. The SP wave propagates on the boundary between metal and dielectric and attenuates exponentially in the dielectric. Surface plasmon can be inspired optically at a metal dielectric interface, only when the wave vector of the optical wave matching that of the SP mode. In most cases, SP mode cannot be excited directly by a light due to the wave vector of the SP mode usually larger than that of the incident wave. The increasement of the light wavenumber can be achieved by the attenuated total reflection (ATR) or diffraction which can be performed in a coupling device. The most common used coupling structures are prism couplers, waveguide couplers, grating couplers, and fiber couplers[31,32].

For prism couplers, Kretschmann configuration[33,34] of the ATR method take advantages over Otto structure[35] due to its easily accessible geometry with no space between a glass prism and a gold film. Incident light passes through a glass prism and is totally reflected at the base of the glass. As a result, an evanescent field is generated and penetrated into a gold layer. By tuning incident angle, evanescent wave along the

prism-gold interface can be coupled to the SP wave on the surface of the gold film. SP wave can be also inspired by grating couplers. Grating couplers without suffering from a metal thickness are easy-to-make using standard micro- and nano- fabrication. Fiber couplers with the ability of remote controlling and particular the single mode fiber immune to the disturbance of multimode make them extensively used as the coupling scheme. The bandwidth and moderate sensitivity, relative to a prism coupler, and the requirement of theoretical design pose the biggest challenges which need to be overcome. Waveguide coupler resembles the principle of prism couplers, i.e. optical mode propagates in a waveguide core and its evanescent tail penetrates in the ambient medium with low refractive index[36]. When the light goes into the waveguide region with metal film covered, a SP mode can be excited at the outer face of the metal film. Only when the propagation constants of the guided mode and the SP mode are equal, will the coupling condition be fulfilled. Waveguide couplers which are compatible with integration technology have become the most promising couplers.

Various commercial devices based on SPR technology have already been made by industrial companies such as Biacore, a division of GE Healthcare[37,38]. Such devices with adoption of prism couplers offer the detection limit of bulk sensing in the range of 10^{-7} RIU to 10^{-6} RIU and that of surface sensing achieving 1 pg/mm^2. However, its intrinsic volume is not compatible with the miniaturization in a lab-on-chip platform and portable device. Moreover, how to improve the sensitivity and resolution of a conventional SPR becomes a focus to the researchers. Nowadays, on the basis of the conventional SPR， modified technologies including localized surface plasmon resonance (LSPR)[39], long range surface plasmon (LRSP)[40], and surface plasmon resonance imaging (SPRi)[41] have sprung up in the field of biosensing. Specifically, LSPR is a longstudied nanoscale phenomenon of considerable recent interest and therefore we will discuss its working principle and recent achievements in the following section.

3.2 Localized surface plasmon (LSP) based biosensor

When a surface plasmon is confined in a nanoparticle (NP) with dimension comparable to an incident wavelength and the particle's free electrons engaged in the

collective oscillation, and it is named a localized surface plasmon. The LSP which is nonpropagating surface plasmon is distributed in a small region near the particle surface and the LSP resonance can be adjusted by the particle properties, i.e. size, shape, and composition[42]. The electric fields near the particle surface are strongly enhanced and the enhancement decaying rapidly with distance. The optical extinction of the particle reaches the maximum value at the frequency of plasmon resonance, which always appears at visible wavelengths for noble metal particle. The extinction peak which is determined by the refractive index of the ambient medium is the foundation for biosensing[43]. Different types of nanoparticles have been reported to enhance the SPR signal in the case of detecting interested and hard–to-find targets, i.e. gold or silver NPs[44-46], magnetic NPs[47,48], carbon-based NPs[49,50], latex NPs[51], and liposome NPs[52]. Amongst which metal NPs are the most preferable and promising material, we will illustrate their recent advances in the following content.

LSPR of the gold NPs is determined by the NPs' size, shape, composition and the refractive index of environment. In particular, it has been announced that in an assembly of Au NPs, one particle is able to interact with an adjacent particle in close proximity via their near-field, which also coupling the plasmon oscillation together. Thus, the interparticle plasmon coupling greatly improves the spectroscopic signal of molecules attached on the NPs and puts the basis of single-molecule detection. EI-Sayed *et al.*[53] first studied the distance decay of plasmon coupling in metal NP pairs and established a plasmon ruler equation. Alivistors *et al.*[54] proposed a reversible plasmon ruler, an aggregation of two Au NPs linked by a single aptamer, which specifically bound target secreted molecules (**Figure 5**). With the two gold NPs getting very closer, the near-field of individual particles would couple and thus generate a light scattering spectrum which was strongly determined by the interparticle distance. Due to the large scattering cross-section of NPs, high intensity of the scattered spectrum can be gained and thus single molecules can be detected with a high spatial resolution. The aptamer bound with target molecules underwent conformational change, resulting in a change in the interparticle distance of the plasmon ruler, which was subsequently observed in the light scattering spectrum.

View Article Online
DOI: 10.1039/C9AN01998G

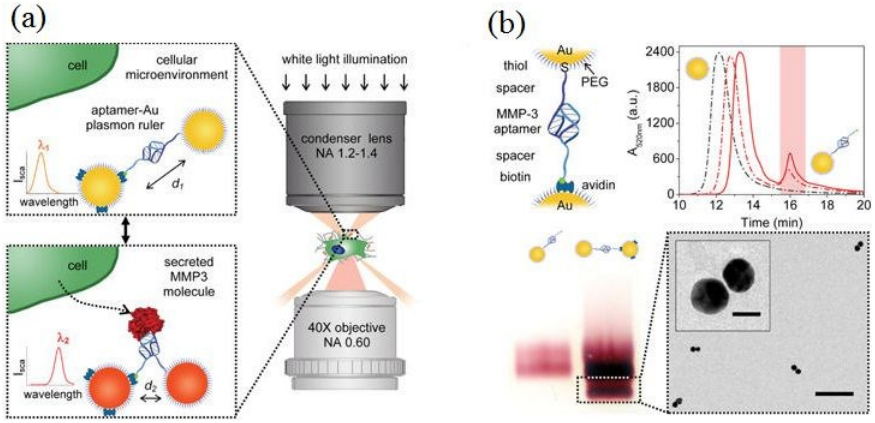

Figure 5. Reversible aptamer-Au plasmon ruler strategy to detect secreted single molecules. (a) Reversible aptamer-Au plasmon ruler. (b) Assembly of reversible plasmon rulers. Reproduced from ref. 54 with permission from [American Chemical Society], copyright [2015].

Moreover, a LSPR effect of noble metal NPs generates an enhancement of the Raman scattering signal from the molecules bound to the surface of NPs. Such phenomenon is named Surface-enhanced Raman (SER) effect[55]. Researchers engaged in decorating Raman active molecules on the surface of NPs, i.e. Raman microprobe, which is used for the detection of molecular target with high specificity and sensitivity. In 2017, Song *et al.*[56] proposed a gold-silver nano-mushroom, silver-containing metal nanostructure with strong and stable SERS signals (**Figure 6**). The oriented growth of silver on the surface of AuNPs attached with DNA molecules caused the formation of interior nanogaps between the silver cap and the gold head in a dimension range of 1-2 nm. Such micro-structure with ability to display well-defined Raman fingerprint peaks, provided potential for ready-to-use SER probes for ultrasensitive and multiplex DNA/RNA detection. In the experiment, synthesized miRNA-21 molecules were used as target analytes with concentration in the range of 10 fM to 100 pM and the DL achieved the value of 10 fM.

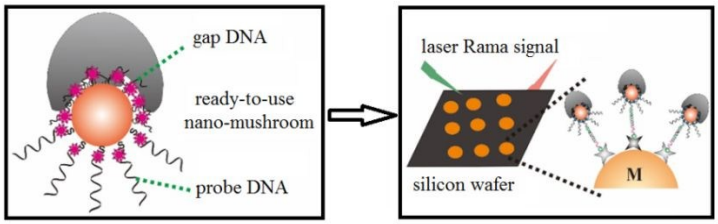

Figure 6. The Au-Ag nano-mushrooms were used as ready-to-use SERs nanoprobes in the detection of DNA molecules. Reproduced from ref. 56 with permission from [American Chemical Society], copyright [2019].

Recently, fluorescence enhancement alongside with the surface enhanced Raman effect has been applied in ultrasensitive bioassay. Fluorescence enhancement occurs in the proximity of metals which may interact with both the exciting laser beam and with the radiating fluorophores[57]. Briefly, a growth of the spontaneous emission rate associating with concomitant increase in the radiative quantum efficiency is observed in the proximity of metal structures. It arises from the shortening of the fluorescence lifetime which makes a cycling of the fluorophore much faster. The emission intensity is determined by the gap between the metal and the fluorophore. The already reported metal structures were in various morphologies, such as metal nanorod[58], metal nanosphere[59], and metals with irregular shape[60]. Cheng and collaborators[61] prepared two metal mesoporous structures, i.e. hexagonal mesoporous silica (HMS) material individually loading with Ag and Au NPs, formed Ag-HMS and Au-HMS compounds, which were subsequently functionalized by rhodamine derivative (R), by the means of impregnation–reduction. The synthesized nano structures in the dimension of 300 nm were used as chemosensors in the detection of mercury ions (Hg^{2+}) in an aqueous solution. It has been shown that the mass fraction of Ag and Au NPs which were 2 wt.% in both Ag-HMS and Au-HMS compounds presented the strongest fluorescence enhancement with the enhancement factor of 4.58 and 2.93 in the presence of 100 ng/ml Hg^{2+}, respectively. The DL of Ag-HMS-R and Au-HMS-R for Hg^{2+} detecting were 0.9 ng/l and 1.4 ng/l respectively.

Tang and Mei[62] developed an ordered gold nanorod (GNR) assembly in vertical standing array on a glass substrate, leading to an enhanced LSPR effect between adjacent nanoparticles. Fluorescence enhancement by the GNR array efficiently conquered the quenching of the gold nanoparticle in a very close proximity. The LSPR induced fluorescence intensification was distance-determined with the competition between quenching and enhancing by the metal structures. The ordered GNR array was then used for DNA analysis (**Figure 7**). Briefly, when the hairpin-structured single strand DNA (ssDNA) conjugated to the GNR nanoarray, fluorescence intensity achieved the minimal value due to the quenching of gold nanorods located very closely. As the complementary ssDNA hybridized with the ssDNA with hairpin-structure, the

fluorophores were extended away from the GNR array surface. The fluorophores were restored and fluorescent intensity was enhanced consequently. Specifically, the hairpin loop was opened up by the hybridization of the complementary ssDNA and a formation of duplex DNA structure with 45-nucleotide-long made the fluorophores about 16 nm away from the array surface. It has been shown that the fluorescence enhancement corresponding to the target ssDNA concentration with a linear relation in a range of 10 pM to 10 nM. The detection limit was determined to be 10 pM.

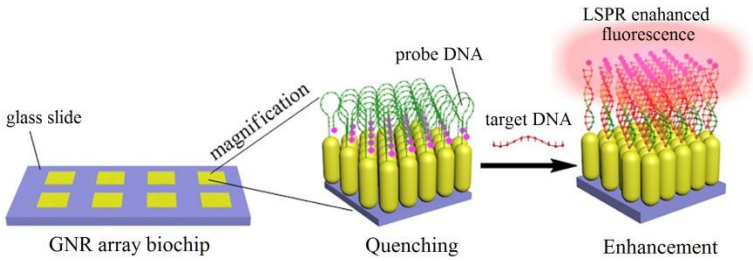

Figure 7. The ordered GNR array chip was used for DNA detection based on surface plasmon enhanced fluorescence. Reproduced from ref. 62 with permission from [American Chemical Society], copyright [2017].

Wansun Kim *et al.*[63] recently reported a cellulose SER biosensor chip decorated with PH-adjusted Au-NPs, which were used for identification of subarachnoid hemorrhage (SAH)-induced cerebral vasospasm and hydrocephalus. The working platform was shown in **Figure 8**. The Au-NPs with positive charges tuned by PH level were synthesized onto a negatively-charged cellulose substrate with zeta potential of -30.7 mV, thereby forming the SERs biosensor chip. The Au-NPs were uniformly and densely distributed over the cellulose substrate due to the strong absorption of a positively charged reactive nanoparticle seed ion (Au^{+}). The LSPR effect was maximized by the means of the optimized design and analysis of zeta potential, nanostructural properties, nanocrystallinity, and electromagnetic field distributions of Au-NPs. The Raman activities of the proposed biosensor were improved with an enhancement factor of 3.29×10^{9} for the analytic concept with reproducibility of 8.5% relative standard deviation. The detection limit of the biosensor achieved the value of 0.74 pM. It has been demonstrated in terms of experimental results that the biosensor was able to identify and predict SAH-induced cerebral vasospasm and hydrocephalus complications with 91.1% reliability and 19.3% reproducibility and thus to promote it

View Article Online
DOI: 10.1039/C9AN01998G

as commodity for neurosurgical diagnosis.

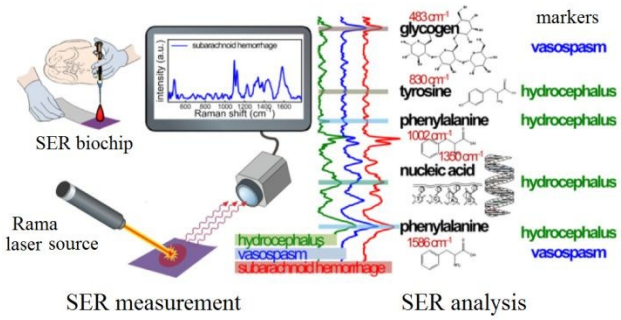

Figure 8. The SER biochip was used for the identification of components in an extracted cerebrospinal fluid so as to rapid diagnosis of vasospasm and hydrocephalus after SAH. Reproduced from ref. 63 with permission from [Elsevier B.V.], copyright [2016].

Andreea Campu *et al.*[64] developed a paper-based nanoplatform for promoting multimodal biodetection by the means of LSPR, SER and metal enhanced fluorescence (MEF). The platform with modulated LSPR responses was deposited by gold nanobipyramids (Au-BPs) onto the cellulose fiber through plasmonic calligraphy approach using a commercial pen (**Figure 9**). Initially, a previously synthesized p-aminothiophenol@Biotin system, which was active receptors for streptavidin binding, was immobilized with the nanoplatform. Three sensing techniques were successfully used for the detection of target proteins. Briefly, LSPR induced by the change of the environmental refractive index after each step was observed as successive red-shifted wavelength in 13-18 nm on the basis of LSPR sensing. Utilizing the ultrasensitive SER technique, biotin-streptavidin recognition was indirectly confirmed by the protein fingerprint bands. In the MEF nanoplatform, the biotin-streptavidin complex served as a spacer to guarantee an optimal distance between Au-BPs surface and the Alexa 680 fluorophore and thus achieved a twofold enhancement of fluorescence emission of strepatvidin@Alexa 680 on the biotinylated paper, compared with the same complex on bare paper. Afterwards, the researchers integrated multiple LSPR, SERS, and MEF nanosensors with multiplex capability into a single flexible and portable plasmonic nanoplatform, which would make the portable point-of-care diagnostics possible.

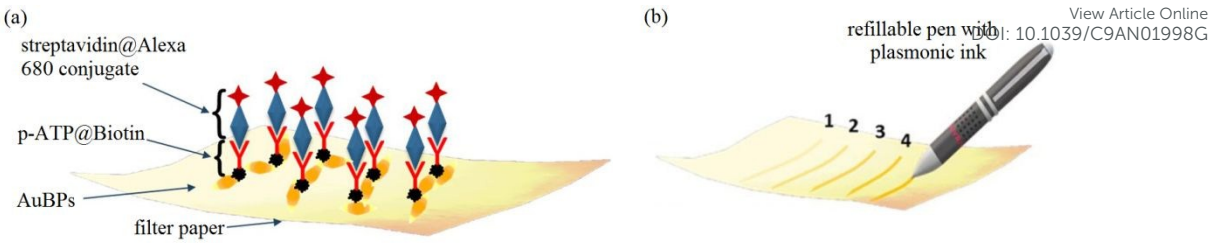

Figure 9. (a) Protocol of a paper-based nanoplatform with modulated LSPR responses due to the deposition of gold nanobipyramids (Au-BPs) onto the cellulose fiber. (b) Schematic illustration of drawing process used a commercial pen filled with AuBPs so as to write different numbers of plasmonic lines. Reproduced from ref. 64 with permission from [Frontiers Media S.A], copyright [2007-2020].

3.3 Optical waveguide based biosensors

Optical waveguide is normally constructed on a substrate with thin thickness and low refractive index using silica or polymer materials. According to the morphology, optical waveguide can be classified as: slab waveguide and stripe waveguide[65]. The difference between which optical waves are confined in the transverse (only thickness direction) of the former configuration, while in the latter structure light can only propagate longitudinally along the waveguide. Stripe waveguide is subdivided into stripe-loaded waveguide, ridge/rib waveguide, buried waveguide, and diffused waveguide, which can be implemented by the standard micro-and nano-fabrication (**Figure 10**). In particular, rib waveguide is common used as a transducer in biosensing. In the principle of evanescent-based detecting, optical wave propagates inside the waveguide film and its evanescent tail penetrates into the cladding layer which is covered by the bulk solution or the target molecules, and senses the refractive index change in the tested sample. Evanescent field is strongly determined by the waveguide dimension and material. Specifically, a waveguide with small size and large value of refractive index difference between guiding film and cladding film provides an intensified evanescent field. Apart from the SOI material which is compatible with a mature processing technology, silicon nitride characterizing with a lower propagation loss and a higher field confinement in the near-infrared spectrum recently performs an increasing potential to be applied in the production of waveguide[66]. Evanescent-based mechanism promotes optical waveguides being developed as biosensor, which frequently adopted configurations are rib waveguide, slot waveguide, and photonic

waveguide. We will give a well-informed discussion of the slot waveguide biosensor and interferometer whose sensing arm is usually present in the form of rib waveguide.

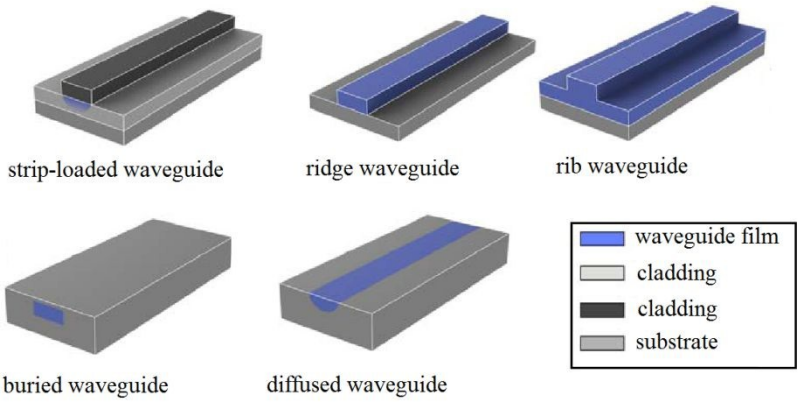

Figure 10. Schematic illustration of different stripe waveguide types. Reproduced from ref. 65 with permission from [Elsevier B.V.], copyright [2014].

3.3.1 Slot waveguide biosensors

Slot waveguide is formed when two slab waveguides with high refractive index are located very proximately and the gap between two waveguides is filled with the medium with low refractive index[67]. Light is confined in the lower refractive index area due to the discontinuity of the normal component of the electric field at the interface. The optical wave passing through the slot is different from the guided wave propagating in the normal waveguide, which exhibits characters of both guided mode and radiation mode. Since light will couple from one waveguide to another, during which the electromagnetic field redistributed in the surroundings and gradually tended to be stable. Evidently, the slots are able to store electromagnetic energy resulting in subwavelength optical guiding with low propagation loss. Since the dielectric discontinuity at Si core/solution interface produces a polarization charge which interacts with the plasma oscillations of the metal-solution interface[68]. The gap region can be equated with an effective optical capacitance resulting in strong field confinement and low propagation loss. Slot waveguide is compatible with CMOS (Complementary Metal-Oxide-Semiconductor) technique and thus integrated in a resonator and an interferometer and made a lab-on-chip platform available. Barrios *et al.*[69] firstly reported a resonator with slot waveguide used for bulk sensing (**Figure 11a**). Drops of solution with varying refractive indices were added on the open window by a micropipette. By monitoring the resonance redshift, the experimental result of

sensitivity was 212 nm/RIU, and that of LOD was 2×10^{-4} RIU. Carlborg *et al.*[70] demonstrated an integrated sensor array based on eight slot waveguide ring resonators, amongst which two resonators were used as reference channels for drift compensation and control experiments, and the rest of which were used for multiplexed real-time label-free biosensing (**Figure 11b**). The detection limit for a volume refractive index was 5×10^{-6} RIU and that for a surface mass density was 0.9 pg/mm^2. Recent years, a multiple-slot based resonator for biochemical sensing was theoretically demonstrated by Khodadad and colleagues[71]. This sensor was able to achieve the sensitivity value of 912 nm/RIU (**Figure 11c**). Pan *et al.*[72] designed a sensor based on a cross-slot waveguide, which contained both vertical and horizontal slots and thus supported dual polarization in the slot region (**Figure 11d**). This novel configuration was superior to the most slot waveguides which were strongly polarization dependent.

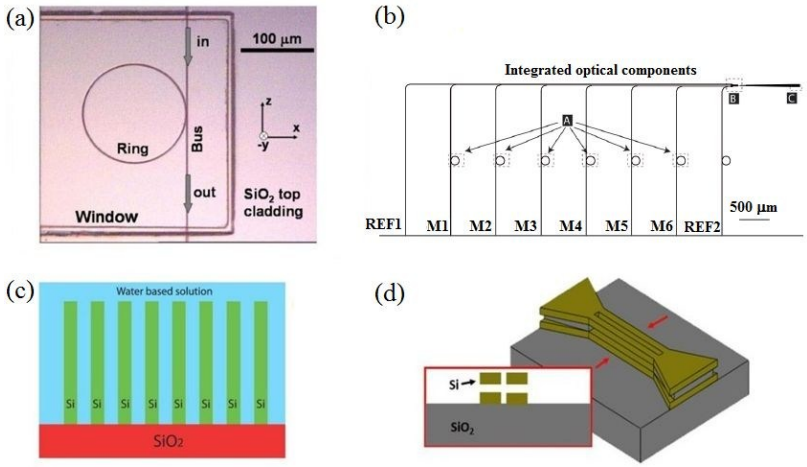

Figure 11. (a) A slot waveguide resonator biosensor. Reproduced from ref. 69 with permission from [Optical Society of America], copyright [2007]. (b) A packaged slot waveguide resonator sensor array. Reproduced from ref. 70 with permission from [Optical Society of America], copyright [2010] (c) A multi-slot waveguide biosensor. Reproduced from ref. 71 with permission from [Optical Society of America], copyright [2014]. (d) A cross-slot waveguide biosensor. Reproduced from ref. 72 with permission from [IEEE], copyright [2020].

Slot waveguide is not only capable of being constructed in the resonator, but also in the optical interferometry and photonic crystal. Sun *et al.*[73] reported a Mach-Zehnder Interferometer (MZI) with double-slot hybrid plasmonic (DSHP) waveguide as active sensing arm for bulk sensing (**Figure 12**). In the DSHP waveguide, two open nano-slots were formed between a silicon layer with high index and two silver layers.

The experimental sensitivity for detecting different concentration of 2-propanol (IPA) solution reached the value of 1061 nm/RIU. Di Falco *et al.*[74,75] combined the slot waveguide with photonic crystal and constructed a cavity based sensor. The fabricated configuration presented a high (Q-factor) of 50000 in air. For bulk sensing, they obtained the limit detection from a Q = 4000 and S = 1538 nm/RIU in their experimental conditions.

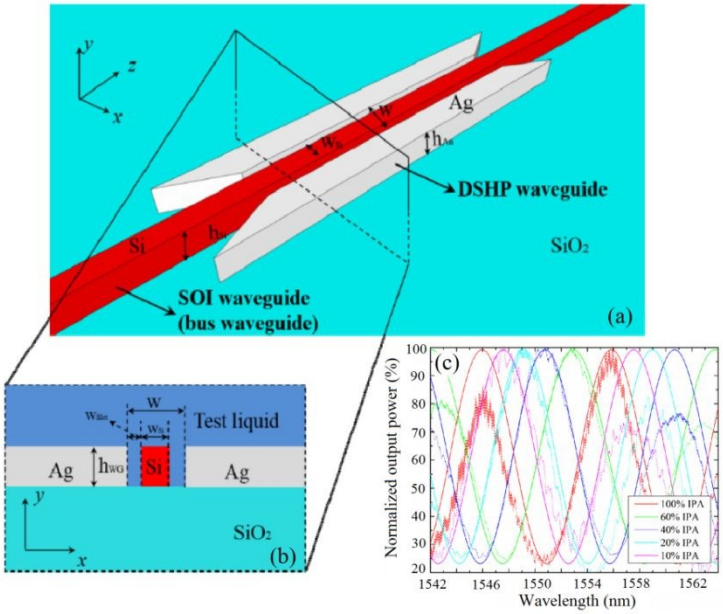

Figure 12. (a) Schematic of the double-slot hybrid plasmonic (DSHP) waveguide. (b) Cross-section view of the DSHP waveguide. (c) Normalized output power of the integrated MZI with DSHP waveguide for various IPA concentrations. Reproduced from ref. 73 with permission from [Optical Society of America], copyright [2015].

3.3.2 Interferometric waveguide biosensors

The waveguide interferometers follow a basic working principle: a guided mode is propagating in a waveguide, while its evanescent field is penetrating into the ambient medium, where any change of the bulk refractive index or the adsorption of a biolayer induces phase shifts of the mode. By combining a phase shifted mode with a reference one, an interference signal can be measured at the sensor's output and subsequently, be processed to the concentration of the analyte. Because of the smart combination of the waveguiding and the interferometry techniques, the interferometric waveguide was developed as a next generation of biosensor. Here, we will illustrate three typical interferometer, i.e. MZI, Hartman interferometer, and Young interferometer, which are applied in the field of biosensing.

View Article Online
DOI: 10.1039/C9AN01998G

(1) MZI biosensor

In a MZI configuration, a monochromatic source is split into two beams, which propagate independently in the two interferometer arms, one of which interacts with the test sample, named sensor arm. Any change of the sample makes a phase-shift of the beam in the sensor arm, while the phase remains constant in the reference arm, which is either isolated from the environment or filled with buffer solution. An interference of the two beams is produced when they recombine, and subsequently transformed to the change of the field intensity, from which the concentration of the sample or the mass density of the adsorbed analyte can be obtained[76]. According to the coupling manner of a light source, one can differentiate between fully integrated MZI interferometer and hybrid MZI interferometer. For a fully integrated MZI, light is coupled into the interferometer by end-fire coupling or by grating coupling, which causes a relative complicated fabrication due to a complex surface structure. A hybrid MZI means that the splitting and recombination of the two beams are done via extra optical elements off-chip, which makes it more sensitive to the mechanical vibrations.

In the early 90s, Heideman *et al.*[77] demonstrated a hybrid MZI interferometer used for an immunoassay, whose sensitivity for the bulk refractive index was 4×10^{-6} RIU. In the same year, a fully integrated MZI interferometer was published by Ingenhoff *et al.*[78], whose work was continued by Prieto and colleagues[79], who presented an optimized configuration with a limit of detection 7×10^{-6} for bulk sensing. In a traditional MZI, sinusoidal nature of the transfer function makes the sensitivity oscillate between a maximum and a minimum value. The maximum sensitivity appears at the maximum value of slope of the sinusoidal curve, while the minimum one appears at the quadrature point of the curve. In the experiment, the initial phase difference between two arms should be adjusted to make the light source match with the sensing structure. Misiakos *et al.*[76] first adopted a broad-band light source to overcome the above problems. The broad-band MZI presented a bulk sensitivity of 20 μm/RIU and a detection limit of 10^{-6}-10^{-7} RIU. Afterwards, Raptis *et al.*[80] reported a monolithically integrated broad-band MZI in detection of biomolecules by dual polarization. The broad-band source light (i.e. emitting diodes) which was coupled to silicon nitride

waveguides was integrated on one chip. Incident light inspired the guided mode with dual polarization, which was simultaneously separated as TE mode and TM mode without ambiguity via deconvolution in the Fourier transform domain (**Figure 13**). It has been demonstrated that the detection limit for multi-analyte sensing reached the value of the order of pM. Chips with similar integrated MZI structure were presented for biosensing by Gajos *et al.*[81,82] in the year of 2016 and 2018, respectively (**Figure 14**).

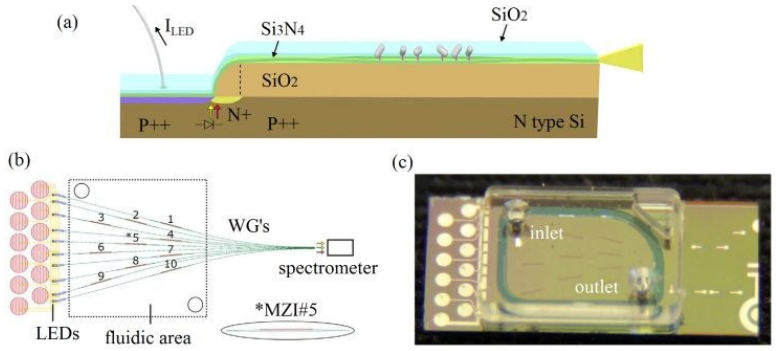

Figure 13. (a) Schematic illustration of a monolithically integration of the avalanche-types LED, the MZI, and the silicon nitride rib waveguide. (b) Layout of the ten MZIs presenting the location of the LED and the routes of the MZI. (c) Photography of the chip with fluidic unit which has both inlet and outlet for the supply of the sample. Reproduced from ref. 80 with permission from [Springer Nature Limited], copyright [2020].

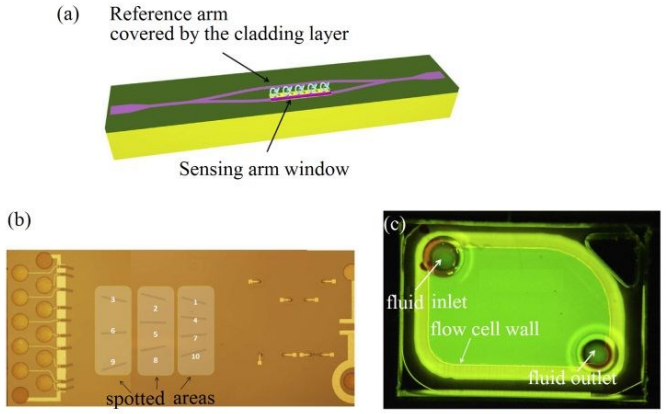

Figure 14. (a) Graphic illustration of the broad-band MZI presenting the sensing window located in the sensing arm. (b) The biosensing chip consists of ten planar nitride silicon waveguide MZIs. (c) Fluidic cell filled with a green fluorescent dye solution. Reproduced from ref. 81 with permission from [Elsevier B.V.], copyright [2016].

(2) biosensor based on a Hartman interferometer

As mentioned above, complexity of sensor surface of a fully integrated MZI

required much more sophisticated fabrication and high cost. Hartman *et al.*[83] endeavored to simplify the sensor surface and demonstrated Hartman interferometer, which comprised of a broad input grating used for coupling an incident light into the chip, multi-sensing regions of waveguiding film, and optical element to collect the light propagating through the adjacent regions and to produce the interference signals. In the year of 1997, Schneider *et al.*[84] made use of Hartman interferometer to detect pathogen, nucleic acid and protein molecules. Afterwards, in the year of 2000, the same group reported the utilization of Hartman interferometer in immunosensing application[85]. Actually, the proposed configuration did not solve the problem of complexity of sensor surface and finally, the concept was no longer promoted.

(3) biosensor based on a Young interferometer

In a Young interferometer, two beams respectively passing through a sensing and reference arms interfered mutually thereby producing interference patterns in the far-field. In this way, sensitivity fading caused by intensity variation can be overcome. A remarkable Young interferometer configuration is the dual polarization interferometry (DPI), which is a simplified slab waveguide system, in which guided modes are confined in only one transverse direction, while lateral modes are infinite[86]. The reference layer is vertically stacked under the sensing waveguide which is exposed to the sample. Two beams passing through both waveguiding films promote interference pattern, which can be obtained in the far field (**Figure 15**). The strength of DPI is that polarization can be switched so as to allow instantaneous measurements of molecular interaction.

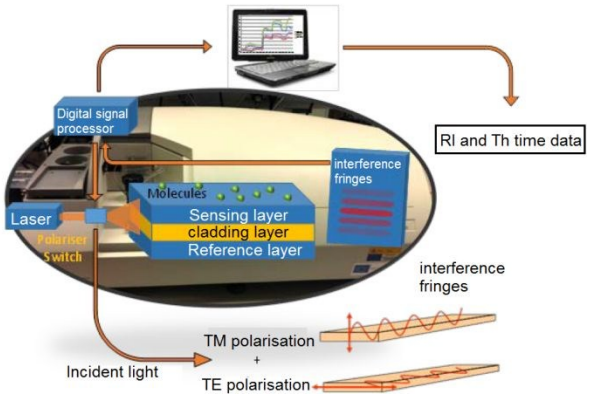

Figure 15. Sketch of a typical DPI. Reproduced from ref. 86 with permission from

[American Chemical Society], copyright [2015].

Recent years, researchers devoted much more time to integrate DPI with other techniques. Ouberai *et al.*[87] adopted a combination of DPI and quartz crystal microbalance with dissipation (QCM-D) and researched on the adsorbed protein. Different protein layers at the interface of liquid and solid were characterized according to parameters, i.e. surface coverage values, layer structure, water content and viscoelastic properties, which were extracted by the incorporated technique. Liang *et al.*[88] took advantages of DPI and ellipsometry to investigate DNA hybridization chain reactions in different salt concentrations at solid-liquid interfaces. They found that sodium ions strongly neutralized negative charges from DNA strands, causing massive aggregates of initiator ssDNA on the interface. At low salt concentrations, ssDNA initiators were distributed uniformly on the surface and extended into the solution. While at high salt concentrations, they aggregated on the surface at the beginning of the immobilization process, and the approaching ssDNA enforced the pre-immobilized ssDNA on extending into the solution.

Apart from DPI, Brandenburg *et al.*[89] built a modern version of a Young interferometer, which was used for a specific biological system, i.e. the reaction of IgG molecule with protein G. A CCD line camera was located at the output of the device to receive a fringe pattern, which was related to the refractive index change in the molecular interaction. The minimum detectable signal response of effective mode index was 9×10^{-8} and the observed detection limit was 0.75 pg/mm^2. Ymeti *et al.*[90] proposed an interesting four channel Young interferometer, which was consist of four waveguide channels located at different distances from each other. The distance between channels produced different spatial frequencies of the interference patterns and thus the path length difference among the four channels was determined. The novel structure was used as an immunosensor, whose determined path length difference was caused by a protein adsorption on the waveguide surface. Proteins were loaded on the waveguide surface via the measuring windows. It has been shown that the refractive index resolution was 6×10^{-8}, corresponding to a protein mass density of 20 fg/mm^2. Schmitt *et al.*[91] proposed a sensor chip based on a Young interferometer. Incident light from a

super luminescent diode was coupled into the chip via one grating, and then propagated in the reference branches and sensing branches, which were decorated with capture molecules, and finally passed a double slit and promoted an interference pattern. The resulting interference pattern was recorded by a CCD camera and read out by a Fast Fourier Transform (FFT) algorithm. It has been shown that the detection limit reached the value in the range of picomole, which was one order of magnitude smaller than that of DPI mentioned above. Two years later, the performance of the proposed sensor chip was improved[92], i.e. the detection limit for bulk sensing was 9×10^{-9} RIU and for surface sensing was 0.013pg/mm^2.

In order to get all the interference patterns, the required distance between waveguide and optical elements was several centimeters, which properly made the interference pattern ambiguous. An extra cooling unit was required to maintain a higher signal-to-noise ratio, thereby increasing the cost. Such weakness has stunted the application of DPI in the point of care (POC).

3.4 Optical resonator based biosensors

Optical cavity which makes light oscillate in an optical circuit, has presented attributes, such as high speed, flexibility, low cost, multi-analyte detection and compatibility with extra optical elements[93]. When light is confined and interferes with itself in a cavity, only specific optical frequencies, named resonance frequencies, can be supported within the cavity without suffering large losses. The micro cavity serves as an optical signal transducer, which is primarily attributed to a change of cavity geometry or material, for instance, caused by deforming or heating the cavity, and thus altering the resonance parameters, which is finally transformed as a change of light intensity. The optical cavities can be classified as Fabry-perot (FP) micro cavity, whispering gallery mode (WGM) resonator, asymmetric cavity, and photonic crystal cavity. Q-factor is extensively adopted in evaluating an optical cavity[94]. A FP cavity possesses a higher Q-factor, nevertheless its intrinsic footprint, and the demands of an expensive cavity mirror and a complex stabilizer, seriously impede its development and application. Recent years, WGM resonators are experiencing a surge in the application of biomedicine and clinical diagnosis. With the advance of nanotechnology, various

materials were used to fabricate the WGM resonators, such as glass, polymer, and semiconductor material[95]. The cavity geometries were designed in different shapes, such as microsphere, toroid and disk[95]. We will discuss biosensors based on WGM resonator in the following section.

3.4.1 Basic theory of WGM resonator

Principally, whispering gallery modes reside in the cavity dependent on the total reflection at the external cavity interface[96]. According to the Snell law, when the refractive index of a dielectric cavity is larger than that of the ambient medium and the incident angle exceeds the critical angle of the total internal reflection, light is confined in the cavity. For the high-symmetric structures, e.g. spherical resonators, the electric field and resonant frequencies can be obtained analytically, and expressed mathematically as below[96]:

$$2\pi R_{WGM} = m\frac{\lambda}{n_{eff}} \quad (2)$$

where, R_{WGM} represents a radius of the cavity, λ is the resonance wavelength, n_{eff} is the effective mode index of the WGM mode, and m denotes the polar order of the WGM modes. As an optical path difference arising from the round trip of the light around the cavity equals an integer multiple of the wavelength, the WGM mode will interfere with an incoming light leading to an enhanced resonance.

3.4.2 Properties of WGM resonator

To describe a WGM resonator, several primary parameters should be taken, including transmitted power $P_{out}(\omega)$, free spectrum range (FSR), full-width at half maximum (FWHM), and Q-factor. Transmitted power $P_{out}(\omega)$ is defined mathematically as the following expression [95]:

$$P_{out}(\omega) = P_0\left[1 - K\frac{(FWHM/2)^2}{(\omega-\omega_0)^2 + (FWHM/2)^2}\right] \quad (3)$$

where P_0 is input power; K is the coupling coefficient; ω_0 is resonance frequency; and FWHM is the full width at the half maximum of the resonance spectrum profile. Coupling coefficient determines how much energy coupled into the cavity. When K equals to 1, the critical coupling occurs. The condition which the amount of light

coupled into the cavity is comparable to that escaped from the cavity during a round trip. It is easier to observe a resonance phenomenon at the critical condition, which is achieved by tuning the gap between bus waveguide and resonator with regard to the waveguide-coupled-resonator system.

Free spectrum range (FSR) is the spectral distance between two consecutively adjacent resonance peaks. The FSR depends on the dimension of the cavity, i.e. a large cavity presents dense spectrum, while a small resonator has a broadly spaced spectrum. The parameter FWHM depends on the total optical losses in a cavity which is described mathematically as[96]:

$$FWHM=FWHM_{ab} + FWHM_{bend} + FWHM_{rough} \quad (4)$$

where $FWHM_{ab}$ denotes the loss coming from the absorption of cavity material and ambient medium, $FWHM_{bend}$ is the bending loss caused by the curvature of a resonator, and $FWHM_{rough}$ represents the scattering loss dependent on a surface roughness, which is mainly brought by the fabrication tolerance and is aggravated in a LSPR enhanced micro cavity.

The Q-factor is widely used in the assessment of a resonator and is defined as[96]:

$$Q = \frac{\lambda_{res}}{FWHM} \quad (5)$$

in which λ_{res} is a resonance wavelength. The Q-factor depends on the cavity material and geometry. The Q-factor which is resulted from the radius of the resonator plays an essential role in determining the magnitude of the resonance shift and the resultant biosensing capability. Typically, a larger cavity possesses a higher Q-factor. A smaller cavity presents a lower Q-factor but a larger resonance shift. Wavelength interrogation which was widely taken to interpret biological event is determined by the radium of the cavity and the corresponding Q-factor. A resonator with a high Q-factor facilitates the detection of nano-particles due to the sharp resonance peaks, while the nano-particles make the slight perturbations of resonance modes resulting in small shifts of wavelength and consequently the requirement of an extra spectrometer with high resolution. A resonator is superior to other waveguide since it makes a multi-analysis easier[97]. To generate a multi-analyte microsystem, the cavities need to be very small.

However, the Q-factor will be decreased. Thus, the trade-off between Q-factor and resonance shift should be considered based on the specific application of interest.

3.4.3 Biosensors based on WGM resonators

WGM resonators which are presented in different configurations, e.g. microsphere, microring, microdisk, and cylinder can be fabricated in various materials, such as silica, polymers, silicon, silicon nitride, and quartz[98-102]. The examples of cavity geometry are shown in **Figure 16**. We will give a detailed description of the WGM resonator based biosensors in aspect of morphology and material.

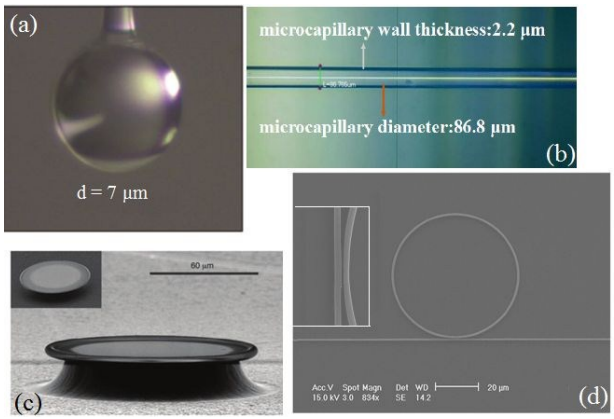

Figure 16. WGM resonators in different configurations. (a) A microsphere bound to fiber. Reproduced from ref. 103 with permission from [Springer Nature Limited], copyright [2020]**.** (b) A micro-capillary resonator. Reproduced from ref. 100 with permission from [The Optical Society.], copyright [2019]. (c) A micro-toroidal cavity. Reproduced from ref. 104 with permission from [Springer Nature Limited], copyright [2020]. (d) A micro-ring resonator. Reproduced from ref. 98 with permission from [IEEE], copyright [2020].

Microsphere resonator which is typically made of glass is usually fabricated by heating and stretching a standard optical fiber and are excited by the same fiber biconical taper[93]. This easy-to-align coupling tool is capable of slightly tuning the propagating mode, which is determined by the taper thickness. An appropriate taper is 1 μm in diameter so that the fundamental mode penetrates into the free space environment and thus promotes fiber mode transferring to a resonance mode. The shortcoming of the fiber biconical taper is its fragile nature coming from the thickness of the taper region. To get rid of this criticality, Conti *et al.*[105] introduced a long period fiber grating (LPG) followed with an adiabatic taper, where cladding modes were inspired in the LPG section and subsequently coupled into the cavity. Microsphere

resonators possess very high value of Q-factor (up to 10^8-10^9) in a visible and near infrared region and thus present spectrums with sharp resonances. As a result, such structures are preferred to detect a single molecule. Recently, Petermann *et al.*[106] proposed an all-polymer microsphere resonator system in which PMMA microspheres were fixed on the PMMA substrate which made the evanescent filed couple into the resonator. Therefore, these novel structures do promote the progress of the commercialization of microsphere resonator.

Toroidal cavity needs an extra geometrical control compared to a spherical shape. They are usually made of silicon glass and thus the process includes photolithography, etching, and lift-off technique. The Q-factor can be achieved up to10^8 by effectively removing the flow in the photolithography and thus perfects for a single-particle detecting. Toroidal cavity is able to be fabricated in a planar array, however, the external coupling system is required thereby weakening the multiplexing capability. Liquid-core optical ring resonator (LCORR) in which light is confined along the perimeter is made by tapering a capillary to the diameters normally larger than 50 μm[107]. It is easier to integrate a LCORR with microfluidic so as to promote the combination being applied in the biosensing. Andres *et al.*[108] proposed a LCORR with a thin and large diameter microcapillary in the detection of glucose solution in various concentrations. They demonstrated that the bulk sensitivity was 850 nm/RIU, and the detection limit was less than 10^{-6}.

Microring and microdisk resonators on a silicon chip are the last category. They can be fabricated in a variety of materials including silicon, silicon oxide, silicon nitride, and polymers[109-112]. The ubiquity of a silicon-on insulator (SOI) wafer which a silica buffer separates a silicon substrate from a silicon waveguide attributes to a compatibility with MEMS (micro electro mechanical systems) technology and NEMS (Nano electromechanical system) technology. Straight waveguides are served as coupling unit, i.e. a guided mode propagates in the waveguide and its evanescent wave inspires a WG mode in a resonator via a specific coupling region. In this way, one straight waveguide is able to associate several resonators thereby implementing the multi-analyte detection. The Q-factor are in the range of 10^2-10^6 corresponding to

different ring radii and materials. Ghulinyan *et al.*[113] reported on the design and fabrication of thin silicon nitride ring resonator (**Figure 17**). The device was based on a strip-loaded structure so as to reduce a light scattering. As a result, the Q-factor achieved the value of 3.7×10^6 in the near infrared wavelength and that of 9×10^5 in the telecom wavelengths. A decade ago, ring resonators were investigated on the fabrication and the first biosensor based on ring resonators was commercially available. Recent years, researchers were dedicated to decorate LSPR nano particles with microring and microdisk resonators. LSPR nano particles can be loaded on the resonator via top-down approach of dedicated lithographic. These hybrid configurations were named hybrid WGM resonators and we will give an elaborate discussion in the following part.

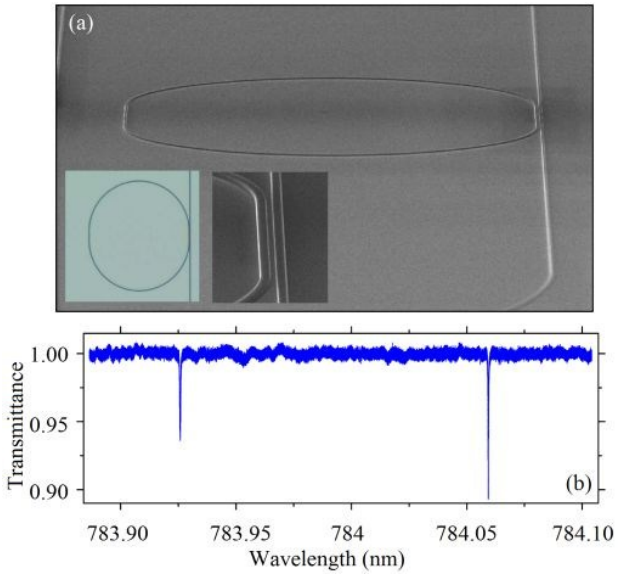

Figure 17. (a) A scanning electron microscope image of the microring resonator coupled to the waveguide. The insets presented the same structure viewed by an optical micro-scope (left one) and an amplified coupling region (right one). (b) The normalized transmission spectrum of the resonator operating in the NIR. Reproduced from ref. 113 with permission from [American Chemical Society], copyright [2019].

3.4.4 Hybrid WGM resonators

For dielectric WGMs, however, only the evanescent tails of the resonant modes penetrate into the carrier fluid, resulting in modest sensitivity (below 200 RIU^{-1})[96]. The introduction of LSPR nanostructures in close proximity to dielectric WGM resonators offers unprecedented sensitivity in the detection of very low concentrations of target molecules[113, 114]. The WGMs provide a resonance mode profile, the key

feature of which is the sensing of perturbations in the ambient medium. Meanwhile, the electromagnetic field is greatly enhanced by the plasmonic component, giving rise to high sensitivity. Two of the proposed configurations for bulk sensing are: (1) a microring with nanostripes or nanodisks along the circumference[115, 116] and (2) a microring (or micro-disk) in a metal–dielectric slot configuration[117]. Plasmonic resonance modes are intrinsically surface waves with longer evanescent tails more accessible to the analyte. Accordingly, the sensitivities of plasmonic resonance modes reach up to 1000 nm/RIU^{-1} for bulk sensing, which is one order of magnitude higher than the sensitivity value of pure dielectric resonators. LSPR nanostructures broaden the width of the resonance peaks thereby reducing the Q-factor of a hybrid WGM resonator compared with that of a dielectric WGM resonator. Nevertheless, the main reason behind the adoption of LSPR nanostructures lies in the detection of single objects. The dimensions of the nanostructure hot-spots (LSPR resonances characterized by a strong field enhancement and confinement) are comparable to that of the target particles, which promotes these LSPR nanoparticles as good candidates for single-object detection. Various configurations of microspheres and microtoroids with metallic nanoparticles, such as gold nanorods and gold nano-triangles, have demonstrated great promise in the detection of single particles and molecules[114, 118]. For example, Vollmer *et al.*[103] proposed a biosensing platform based on a glass microsphere decorated with gold nanorods and used for the detection of nucleic acid hybridization, down to single 8-mer oligonucleotides (**Figure 18**). Nadgaran *et al.*[118] theoretically demonstrated a hybrid WGM microtoroids resonator bound with triangular gold nanoprism (**Figure 19**). The proposed structure was used for the detection of single BSA protein and the resonance wavelength shift was 26.45 fm. It was found that the Q-factor was 3.6×10^4.

View Article Online
DOI: 10.1039/C9AN01998G

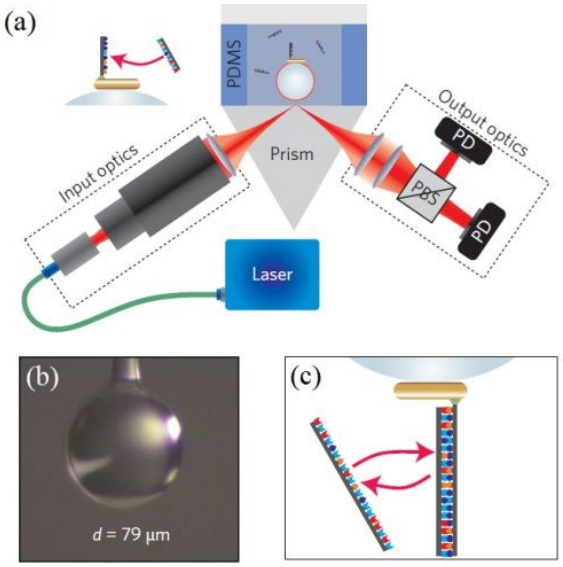

Figure 18. (a) A WGM biosensor platform for single molecule detection. (b) A microsphere is melted from an optical fiber and attached to the short fiber stem for locating. (c) A nucleic acid interacts at the nanorod. Reproduced from ref. 103 with permission from [Springer Nature Limited], copyright [2020].

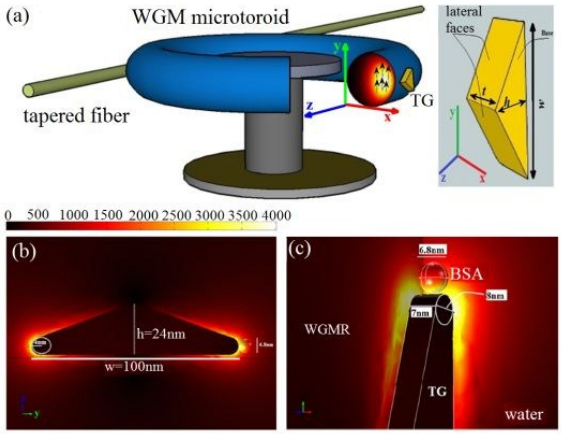

Figure 19. (a) Sketch of WGM microtoroid decorated with a gold triangular nanoprism. (b) Simulation result of a BSA molecule situated top on the triangular gold nanoprism. (c) An amplified image of the overlap of the near field intensity and the dielectric volume in on the top of nanoprism. Reproduced from ref. 118 with permission from [AIP Publishing LLC], copyright [2020].

However, the main challenge is the WGM damping in the metal. Consequently, the amount and the distribution of LSP nanoparticles, which depend on the morphology of the resonator, have to be considered carefully. Another issue is to efficiently improve the Q-factor of the hybrid WGM resonator. In the presence of metal, Q-factor of a hybrid WGM resonator decreases greatly. A WGM resonator is not competitive with a pure dielectric rival. Assuming that sensitivity is improved 4 times in a hybrid WGM resonator at the operating wavelength 1.55 μm, the hybrid configuration should have

an experimental Q factor of 5000-10000 so as to compete with the dielectric resonator counterpart. Instead of metal, materials with lower losses in the visible and near-infraded region might be taken to alleviate this problem. Milliron *et al.*[119] reported on the design and synthesis of a novel doped metal oxide nanocrystal material which displayed a narrow line widths and high Q-factor in a mid-infrared spectrum.

3.5 Photonic crystal based biosensors

Photonic crystal (PC) which stems from the pioneering work of Yablonovitch and John[120, 121] is aimed to create materials to manipulate photons, the way which resembles a semiconductor crystal influence on the properties of electrons. PC consists of two or more materials with different refractive indices which are periodically arranged in the space and manipulates light at the scale of optical wavelength[122]. In the PC structure, photons can be deemed as a band structure, as in the case of electrons. Specifically, a band structure possesses a complete photonic band gap (PBG), i.e. frequency range in which the propagation of light is forbidden inside the crystal. This periodic structure will be broken by the introduction of some defects which causes localized photonic states in the gap, whose shapes and properties are affected by the nature of the defect[123]. Since defects in PC can be designed in the terms of any shape, dimension, one can tune the defect states to any frequency and spatial extent of design interest. Accordingly, it is possible for a PC to provide a strong field confinement, small mode volume, and low extinction loss.

In the last decades, researchers have been dedicated to the development of biosensors based on PC and a variety of devices have been proposed[124-130]. For example, Miller *et al.*[131] proposed a PC waveguide biosensor in the detection of viruses. The biosensor comprised of a 2D PC silicon slab with a triangular lattice of air holes. In order to produce a linear defect, a single array of central air holes was removed. As a result, modes were permitted to propagate through the crystal within PBG. It has been shown that the experimental sensitivity of 0.1nm/nM and the detection limit of 1.4 nM in both buffer and serum solution. Cetin *et al.*[132] proposed a biosensor platform based on PC with nanohole arrays via electron beam lithography and highlighted its applicability in biosensing. Utilizing spectrum interrogation, an experimental detection

limit of 200 pg/mL was shown. Arunkumar *et al.*[133] designed a PC ring resonator based biosensor in the detection of different blood components in whole blood sample. It has been shown that the theoretical detection limit was 0.002 RIU^{-1}. Arafa *et al.*[134] presented a PC based biosensor for glucose concentration detection and made a theoretical investigation via FDTD method. The proposed structure which was constructed in a SOI substrate was consist of a ring shaped PC cavity, coupled to an input and output PC waveguides. The simulation results showed that a sensitivity of 462.61 nm/ RIU and a Q-factor of 10^5, resulting in a detection limit less than 3.03×10^{-6} RIU. Park *et al.*[135] proposed a PC structure which took a hydrogel as a backbone in light of its homogeneous water surrounding (**Figure 20**). An optical microscope with CCD camera was adopted to observe a color change in the PC film and a spectrum analyzer was used to measure a wavelength shift. When the analyte IgG with a concentration of 10 mg/ml was added to the sensor surface, the reflective color was changed from green to dark orange with a PBG shift of 50 nm which is larger than the previous value. Since the color shift was depending on the PBG shift and a narrow bandgap probably could not provide the color change that the human eyes can perceive. Therefore, the novel device was capable of detecting quantitative molecular interactions.

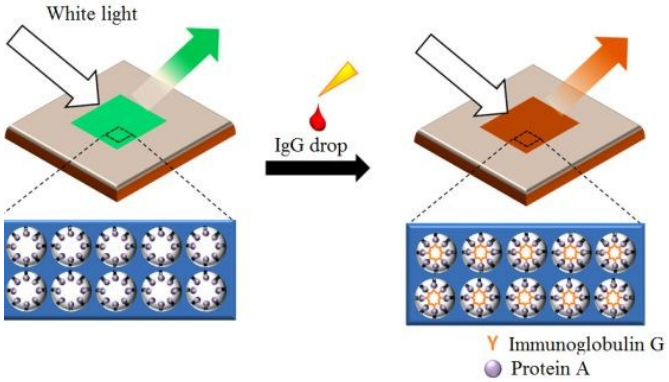

Figure 20. Detection mechanism of the nanoporous hydrogel PC biosensor. It was capable of detecting IgG antibody by observing the color change in dry condition. Reproduced from ref. 135 with permission from [Elsevier B.V.], copyright [2012].

Recent years, PC structures have been extensively applied in microfluidics, telemedicine, smart material, and flexible sensors[136]. The advances in biosensors considerably benefit from microfluidics technology. The strengths are low-cost

material, low sample volume, integration with optical platform, and realization of multiple channels. Particularly, PC integrated with microfluidic facilitates clinical diagnosis and promotes the universality of the POC. As early as 2007, Cunningham *et al.*[137] reported on the design and manufacture a 96-well microplate attached with microfluidics network integrated with PC biosensor. Special detecting instrument was used so that kinetic and imaging measurements were done simultaneously. Scullion *et al.*[138] demonstrated a slotted PC sensor integrated with PDMS microfluidics and connected tubes for solution injection. The device was constructed in SOI substrates by the means of electron beam lithography, reactive ion etching, and hydrofluoric acid under-etching. When the sensor was used in the measurement of dissolved avidin, the detectable concentration achieved as low as 15 nM or 1 μg/ml. For a surface sensing, it has been reported that the surface mass density was 60 pg/mm^2 corresponding to the bound mass of 100 ag.

With advances in smartphone, telemedicine is springing up vigorously[139]. Smartphone which possesses excellent build-in equipment, such as touch screen, multicore processor, and digital camera is now becoming indispensable part in our daily life. The ubiquitous availability ensures an acquisition of smartphone conveniently and thus promotes a potential of smartphone-based sensor in clinical diagnosis. In recent years, smartphone has been intensively combined with sensors, especially optical biosensors due to the presence of a high resolution camera. For example, Gallegos *et al.*[140] first took advantage of a build-in camera which was used as a highly accurate spectrometer in the detection of wavelength shift from a PC biosensor (**Figure 21**). In principle, light from an external source was collimated by a collimator and subsequently polarized and passed through the PC, after which cylindrical lens were positioned so as to intensify the light which will be collected by the camera. The smartphone was held by a cradle in a fixed alignment with optical components thereby guarantee of an exact and repeatable detection. The images were recorded by the camera and afterwards translated into a transmission spectrum by a custom software application. This software worked in the visible wavelength and provided curve-fitting analysis with a wavelength resolution of 0.009 nm. Thus, this handheld biosensor can be developed as a POC

View Article Online
DOI: 10.1039/C9AN01998G

device in the future.

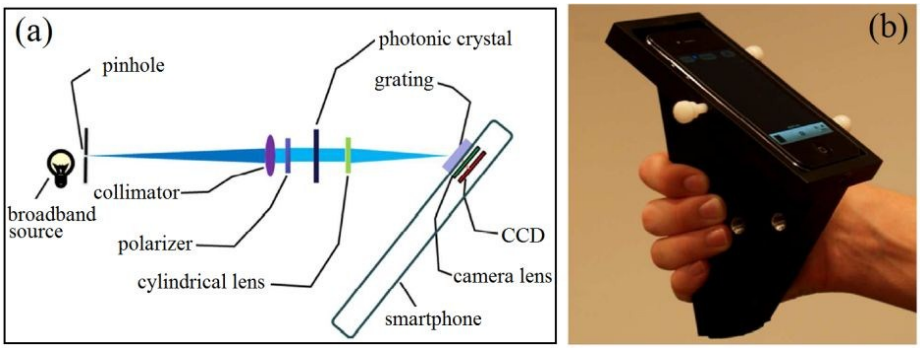

Figure 21. (a) Sketch of the optical components in the smartphone cradle. (b) Photo of the cradle with a PC biosensor inside. Reproduced from ref. 140 with permission from [Royal Society of Chemistry], copyright [2020].

Park *et al.*[141] proposed a user-friendly biosensor which can selectively detect influenza A (H1N1) virus with low limit detection of 138 pg/ml. The intact setup was comprised of a sensing unit in which the emission fluorescent signals from quantum dot-aptamer beacons were amplified by the light guiding in a three-dimensional PC, and a build-in camera of a smartphone which captured the fluorescence images with different concentrations of target analyte for diagnosis without location limit (**Figure 22**). The portable device made the assay process much easier and fast, i.e. collecting samples from coughing or sneezing or throat and nasal swabs from flu-infected patients and making a mixture of the targets with the as-prepared quantum dot-aptamer beacons and incubating for 40 min. The total cost of the sensing unit was only 20 US dollars. It is promising to be applied in the field of clinical medicine and pharmaceutical industry.

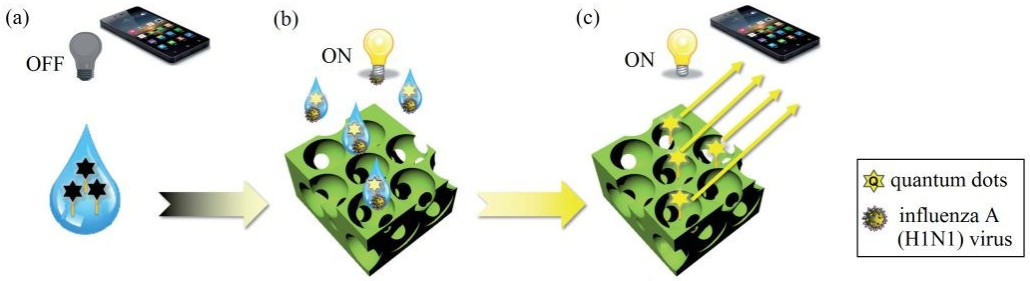

Figure 22. The principle of the "OFF-ON" detection by the means of quantum dots conjugates and nanoporous PC. (a) "OFF" state, i.e. loading the prepared quenched quantum dots conjugates. (b) "ON" state, i.e. capturing H1N1 virus and recovering quantum dots signal. (c) Quantum dots signal was enhanced by the emission light propagating in the PC structure so as to make the virus detection visualized. Reproduced from ref. 141 with permission from [The Royal Society of Chemistry], copyright [2018].

Smart materials, such as hydrogels, graphene, and carbon nanotubes, bring a new surge of researchers' interest, due to their responding nature, i.e. the external stimuli including PH, temperate, electromagnetic field, can change the physical and chemical properties of such materials[142,143]. Particularly, smart materials are incorporated into PC structures thereby promoting a sensitive, fast and trustable sensing strategy. For example, Asher *et al.*[144] synthesized a so-called glucose/galactose binding protein (GGBP) hydrogel which contained a surface attached two-dimensional PC. Shrinkage in GGBP hydrogel caused by a glucose-induced conformational change would reduce the PC particle spacing thereby making blue-shift diffraction. The 2D PC-GGBP hydrogel served as a biosensor which selectively measured glucose concentration in the range of 0.2 μM to 10 μM. Maeng *et al.*[145] presented a three-dimensional inverse opal PC biosensor which was made up of a hydrogel backbone in the detection of Rotavirus. This biosensor was capable of concentration detection ranging from 6.35 μg/ml to 1.27 mg/ml. Combination of two smart materials can create a surprising result. Ge *et al.*[146] demonstrated a one-dimensional PC biosensor, whose building blocks were graphene oxide hydrogels, selectively in the measurement of beta-glucan with the LOD of 0.18 mg/ml. The research groups devoted to the pure hydrogels previously. This time, the researchers deposited the graphene oxide in a silica layer and then implanted into hydrogel. A resultant linear function between photonic band gap and the glucan concentration within 1 mg/ml to 10 mg/ml was clearly shown in the reflection spectra.

An enthusiasm of flexible sensor is inspired by a predicament, i.e. the developed fabrications are commonly based on the silicon-based materials which are rigid; however, the organisms are soft and curvilinear. The incompatibility is resolved by the emergence of flexible material which can be used for manufacturing wearable sensors. Wearable sensors are normally presented in the forms of wristband, skin patches, and fabric patches and have been used to monitor physiological indices, such as the heart rate, skin temperature, and blood oxygen levels. Xu *et al.*[147] demonstrated a microcavity sensor which was made up of a flexible monocrystalline PC structure (**Figure 23**). The sensor could be bent to a curvature of 5 nm radius without scarifying the Q-factor. The device exhibited a Q-factor up to 2.2×10^4 and a sensitivity of 68

nm/RIU under different bending conditions. The deformation-independent sensitivity was crucial for the sensor to be developed as a commercially available wearable device. Very recently, Zhao and colleagues[148] first reported on an integration of microneedle arrays with PC barcodes, which can be inserted into skin and thus enabled a means for painless, noninvasive detection of biomarkers in skin interstitial fluid (**Figure 24**). This strategy was superior to the existing microneedle arrays due to its less post-processing and multi-analyte detection.

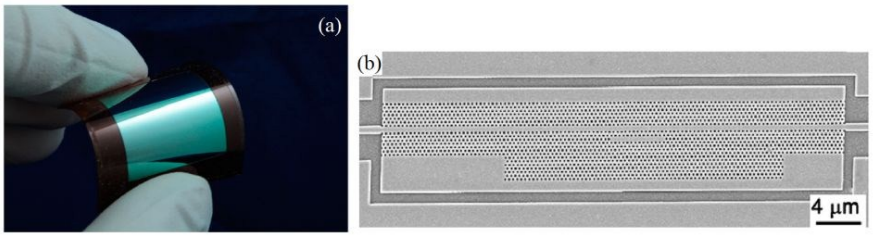

Figure 23. (a) Photo of the proposed microcavity sensor which was made up of a flexible monocrystalline PC structure. (b) SEM image of the PC microcavity. Reproduced from Ref. 147 with permission from [American Chemical Society], copyright [2019].

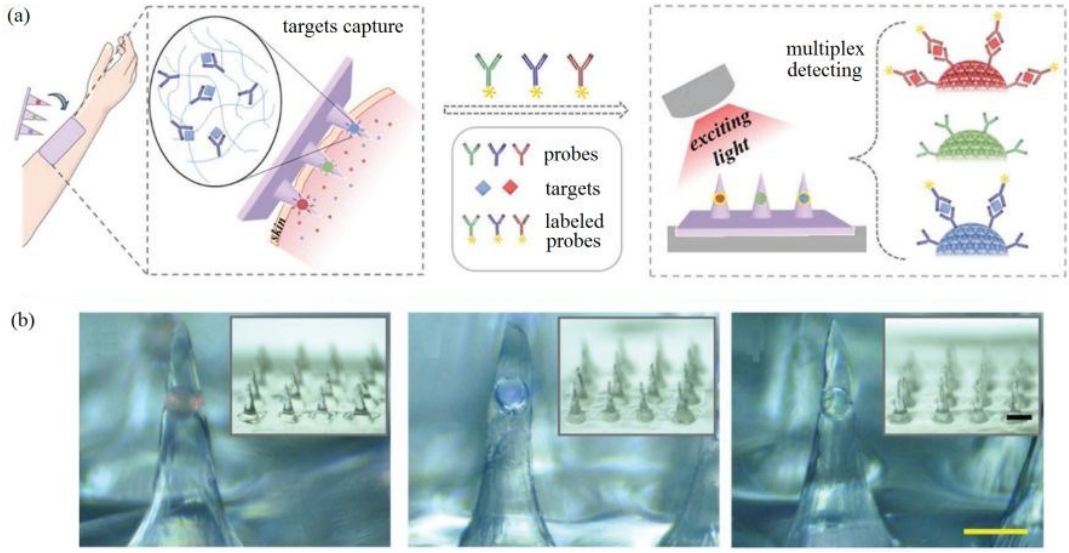

Figure 24. (a) Sketch of application of the proposed microneedle arrays which was integrated with PC barcodes in the detection of biomarkers in skin interstitial fluid. (b) Optical images of the microneedle arrays with one barcode loaded in a single tip. Reproduced from ref. 148 with permission from [John Wiley & Sons.], copyright [1999-2019].

3.6 Optical fiber based biosensors

An optical fiber consists of core and cladding and the refractive index of the core is slightly higher than of the cladding so as to guide an incident light. Extra layers are

introduced as secondary cladding for protecting the fiber[149]. Light satisfying the Snell's law of reflection can propagate in the optical fiber. Accordingly, optical fiber is also referred as "optical waveguide". Only single mode can be guided in the optical fiber which is named single mode fiber. More than two modes can simultaneously propagate in the optical fiber which is called multimode fiber[150]. Optical fiber based sensors have attracted a great deal of attention in different analytical fields, attributing from the nature of optical fiber[151-156] which is susceptible to an external electromagnetic interference and surviving in harsh environment and extreme temperature. Multi-analysis of various targets is allowed due to multiplex of fibers. Because light propagates in single mode optical fibers with low attenuation, they can provide remote detecting and monitoring. Efforts are devoted in the design and detection schemes based on optical fibers so as to create highly sensitive and selective sensors in real practice. To date optical fibers perform in a variety of configuration and in particular tapered optical fiber and fiber grating are the most extensively adopted in the construction of sensors. In the following paragraphs, we will mainly illustrate these two types of sensors, i.e. tapered-fiber optical biosensor and fiber Bragg grating (FGB) based biosensor.

3.6.1 Tapered-fiber optical sensor

To make a tapered optical fiber, one should heat a specific section of the fiber, meanwhile pulling the two ends of the fiber[157]. In this way, the diameters of the core and the cladding are reduced equally which results in coupling of fundamental mode of untapered fiber to the mode of the tapered section and facilitating the evanescent filed more accessible to the surrounding medium and interacting with the target analytes[158]. In detail, the waist which is a region of fiber with reduced and uniform diameter is connected with conical sections with gradually-changed diameter which serve as a transition part between the waist and the original fiber (**Figure 25**). The optical character of the tapered fiber is primarily determined by the dimension of the waist, the profile of the conical section and the ambient medium. Evanescent field is intensified thereby improving the interaction with ambient medium due to the decreasing in diameter of the waist and the decreasing between the refractive indies of the fiber and

ambient medium. Thus, the tapered optical fibers show a great potential to be developed as sensors. Chong *et al.*[159] proposed a non-adiabatic tapered optical fiber sensor for measuring the dye concentration of analyte containing Remazol Black B. Flame brushing technique was utilized to taper the single-mode fiber. In order to get an accurate result, the absorption spectrum associated with the wavelength shift from the same experimental setup was extracted simultaneously. It was shown that the dye concentration within a range of 50 to 250 ppm can be detected with sufficient sensitivities which were 7.61×10^{-5} abs/ppm and 0.0045 nm/ppm respectively derived from the light absorption and wavelength shift. Zibaii *et al.*[160] investigated the dopamine (DA), a neurotransmitter of the central and peripheral nervous system, interacting with dopamine-binding aptamer (DBA) without common interferents, by utilizing tapered optical fiber sensor. DBA molecules were immobilized on the tapered surface of the fiber before ahead. It has been demonstrated that the sensitivity for the measurement of the DA concentrations lower than 1 μM was 0.27±0.05 nm/μM and that of the DA concentrations in a range of 1 to 10 μM was 0.08 ± 0.01 nm/μM. The corresponding detection limits were 37 nM and 125 nM respectively. The superiority of small size, immunity to electromagnetic interference over the previously reported methods, made the proposed sensor a promising technique in analysis of DA in the brain research. Arjmand *et al.*[161] demonstrated a non-adiabatic tapered optical fiber sensor for sensitive and label free detection of organophosphate pesticide (**Figure 26**). The taper region was functionalized with the enzyme acetylcholinesterase via glutaraldehyde, which is a bifunctional cross-linker agent. A standard single mode fiber was used for construction of biosensor because it was compatible with other optical element including light source and optical spectrum analyzer. A customer-made holder was taken to guarantee a good mechanical stability and thus an accurate result. In principle, bulk refractive index change or biomolecular interaction can promote propagation modes interference. The proposed device presented a sensitivity of 2100 nm/RIU by the means of detecting the wavelength shift of the interferometric spectra. Detection limit achieved 2.4×10^{-10}M for the concentration of organophosphate in a range of 10^{-10} M to 5×10^{-5} M. The extra strengths of this biosensor were highly

reproducibility to organophosphate reactivating agent with the relative standard deviation (RSD) of 2.36% and 2.44%, respectively. Thus, this novel biosensor had potential to be developed as a tool for fast, sensitive, cost-effective, and real-time detecting of organophosphate pesticides.

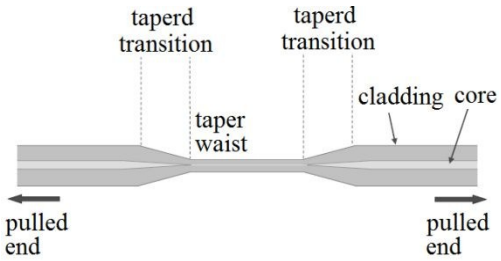

Figure 25. Schematic illustration of the tapered optical fiber which consists of the waist and two conical sections. Reproduced from ref. 158 with permission from [MDPI], copyright [1996-2020].

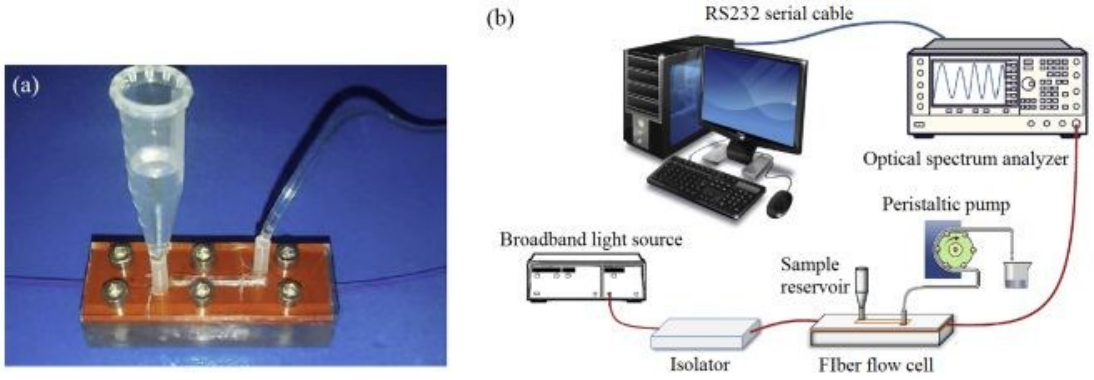

Figure 26. (a) The proposed tapered optical fiber with a specially designed flow cell. (b) The experimental setup in the detection organophosphate pesticide based on the tapered optical fiber sensor. Reproduced from ref. 161. with permission from [Elsevier B.V.], copyright [2017].

3.6.2 FBG biosensor

So far, people have been dedicated to study the fiber grating sensors and some of which have already been commercially available[162-166]. The fiber gratings can be sorted into fiber Bragg grating (FGB), long-period fiber grating (LPG), chirped fiber grating, titled fiber grating, and sampled fiber grating, among which FBG is widespread used in the sensor design[167]. FBGs can be simply "photo-imprinted" into fiber and the resultant FBG sensors are typically sensitive to strain and temperature[168-171]. However, refractive index based sensing cannot be carried on by a FBG sensor because the optical field is confined in the fiber core. To improve this scenario, evanescent field is required to access to the surrounding environment and this can be obtained by polishing, etching,

or tapering the fiber. When the FBG is immersed in a sample liquid, a wavelength response of the Bragg grating which is determined by the bulk refractive index will appear. Assech *et al.*[172] first utilized hydrofluoric acid (HF) to etch the fiber cladding at the position of the Bragg grating which intensified the evanescent field interacting with the ambient surroundings of the fiber. Iadicicco *et al.*[173] proposed a thinned FBG sensor for bulk sensing. The uniformly thinned FBGs were achieved by the utility of wet chemical etching in HF solution which promoted the evanescent field more accessible to the analyte in the surrounding solution and thus the light-matter interaction was enhanced. In order to test the sensor sensitivity, glycerin solutions with well-known refractive indices were adopted in the experiment. It has been indicated experimentally that the proposed sensor was capable of a response to the external refractive indices varying in the range of 1.333 to 1.450. Athanasios *et al.*[174] proposed a etched core FBG sensor with high sensitivity which sensed the external refractive index change by measuring the Bragg wavelength shift. When the fiber core was reduced to a diameter of 3.4 μm and the refractive index of the surrounding environment was close to that of the fiber core, the sensitivity achieved the value of 1394 nm/RIU. When the surrounding index was less than that of the fiber core, higher order modes performed much more sensitive in the detection, i.e. a sensitivity of 404 nm/RIU was obtained with the secondary order mode compared with a sensitivity of 171 nm/RIU with the fundamental mode. Finally, the FBG sensor was used to detect the hybridization of DNA molecule. Single strand DNA oligonucleotides, served as probes, were immobilized on the surface of the fiber grating by the means of common glutarahyldehyde chemistry. Hybridization of target DNA molecules were observed and the wavelength shift of 73 pm was measured, corresponding to the index change of 2.5×10^{-3}. The demonstrated FBG sensor permitted the in situ monitoring of bioprocesses.

Recent years, FBGs have been extensively employed for the measurement of various parameters, such as temperature, refractive index, strain, and magnetic field[175-178]. Tested solution is required to be measured in a temperature-stable condition or else it is difficult to discriminate between refractive index and temperature. Thus, it is necessary to detect bulk refractive index and temperature simultaneously. The

measurement of temperature for compensation by the use of FBG has been proposed. For example, Han *et al.*[179] proposed an all-fiber sensor composed of a FBG cascaded with a droplet-like fiber which was able to simultaneously monitor the change in refractive index and temperature (**Figure 27**). The droplet-like structure was made by mechanically bending a section of coating-stripped fiber at the pigtail section of the FBG. Resonance dips caused by FBG were dependent on temperature and that caused by the droplet-like structure were determined by both temperature and ambient refractive index. Accordingly, by the means of extracting the wavelength shifts of two series of resonance dips, one can simultaneously measure the temperature and bulk refractive index. It has been demonstrated that the experimental sensitivity of 158 nm/RIU for refractive index in a range of 1.333 to 1.3785 and that of 10.3 pm/°C for temperature. Li *et al.*[180] experimentally demonstrated a compact optical fiber based sensor for simultaneously detecting refractive index, strain, and temperature. The sensor was comprised of a four-core fiber with a FBG (**Figure 28**). According to the wavelength shifts of three dips, refractive index, strain, and temperature could be measured at the same time. Changes in the refractive index, strain, and temperature could be obtained by the means of a sensitivity matrix with the corresponding experimental resolution of 0.0004 RIU in refractive index, that of 11.06 με in strain, and that of 0.17 °C in temperature. Thanks to the mentioned advantages, the sensor exhibited great potential for refractive index sensing. Wu *et al.*[181] demonstrated a sensor which was comprised of a D-shaped fiber with etched cladding and a FBG for bulk refractive index and temperature sensing (**Figure 29**). The D-shaped fiber was served as the sensing unit and the resulting interference was strongly dependent on the surrounding refractive index. By monitoring the resonance wavelength shift of the D-shaped fiber and the Bragg wavelength shift of FBG, bulk refractive index and temperature were measured without ambiguous. It was shown that the sensitivity was -31.79 nm/RIU for refractive index ranging from 1.333 to 1.428 and that for temperature was 28.7 pm/°C.

View Article Online
DOI: 10.1039/C9AN01998G

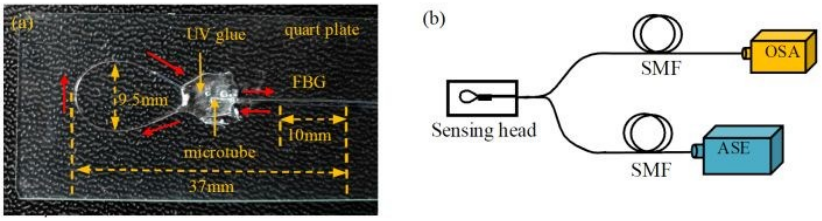

Figure 27. (a) Picture of the fabricated all-fiber sensor which was composed of a FBG cascaded with a droplet-like structure. (b) Schematic illustration of the experimental setup for the simultaneous measurement of the temperature and bulk refractive index. Reproduced from ref. 179 with permission from [IEEE], copyright [2020].

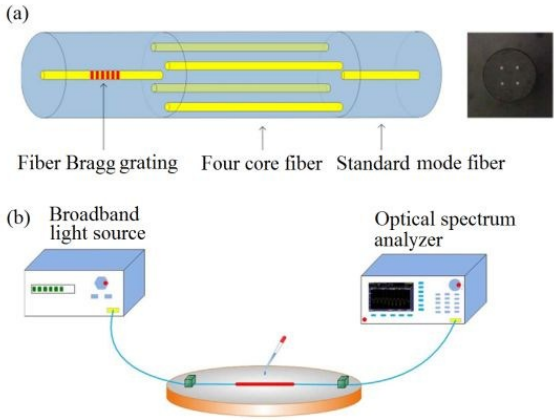

Figure 28. (a) Graphical illustration of the proposed sensor which was comprised of a four-core fiber with a FBG. (b) The experiment setup used for simultaneously detecting refractive index, strain, and temperature. Reproduced from ref. 180 with permission from [Elsevier Ltd.], copyright [2016].

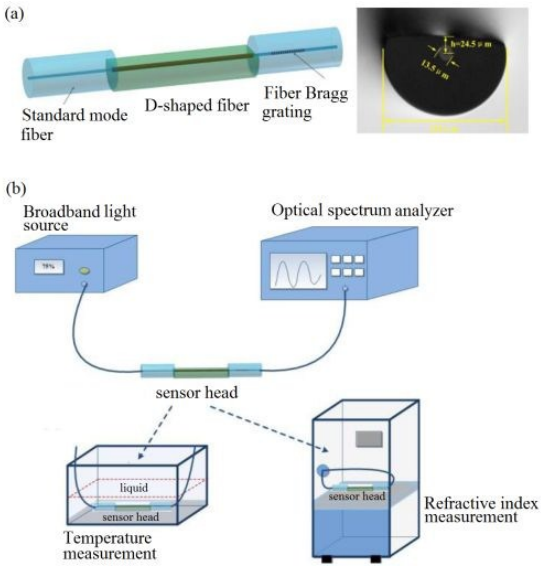

Figure 29. (a) Schematic diagram of the proposed sensor which was comprised of a D-shaped fiber with etched cladding and a FBG. (b) Schematic diagram of the experimental setup for bulk refractive index and temperature sensing. Reproduced from ref. 181 with permission from [IEEE.], copyright [2020].

4. Future outlook

Optical biosensors can be utilized in diverse fields, including clinical diagnostics, environmental monitoring, food quality control and drug discovery[182-186]. Particularly, diagnosis in developing countries could make a great advance for the near future by the use of this advanced technology. During last years, great efforts have been made in the development of biosensors. Since the birth of a mature biosensor definitely demands cooperation between different disciplinary, this area is still in its infancy. Nevertheless, a remarkable progress has been achieved which is proved in the increasing amount of publications addressing new or optimized sensing configurations[187-192]. Some optical biosensors have been introduced into the market, but most of them are bulk and expensive. Complete integration of the sensor and detection in a single chip thereby forming a mechanically-stable, reproducible and user-friendly device is becoming an emphasis in the future investigation. Because intensive investigations have being done, the integrated, miniaturized and portable biosensors will undoubtedly become universal in our daily life and will impact positively our living in near future.

5. Conclusions

In the past decade, optical biosensor technology has made tremendous strides in both sensor configuration and biospecific coatings. Optical biosensors have been utilized in the detection of a variety of chemical and biological analytes. The performance of optical biosensor will continuously evolve and the advanced sensor structure associated with novel biofunctionalized surface immunity against nonspecific binding will lead to robust biosensor with ability to fast, sensitive and specific measurement of targets in complex samples. The biosensors will benefit diverse sectors such as clinical diagnostics, environmental monitoring, food quality control and drug discovery.

Acknowledgements

This work was supported in part by Scientific Research Foundation for Talents, Dalian Maritime University (02500339).

Biography

View Article Online
DOI: 10.1039/C9AN01998G

Chen Chen received her master degree in chemistry (track is biochemistry) from the Organic and Biochemistry Department, Uppsala University, Uppsala, Sweden. She received the Ph.D. degree in Electronic Science and Technology Department, Xi'an Jiaotong University, Xi'an, China. Her research focuses on optical biosensing applied in the field of biochemistry and biology. She has been engaged in the design and manufacture optical biosensors since her master project. In recent years, Dr. Chen as first author has published original research works in the academic journals including Optics Express, Nanotechnology, IEEE sensors journal, and Nanotechnology Reviews. Thus, she has many positives in her biosensor record.

Junsheng Wang holds a Ph.D. in physics in the field of physical electronics of Harbin Industrial University. Currently, he is the professor in the College of Information Science and Technology, Dalian Maritime University. His main expertise relies on photoelectric detection technology and microfluidic chip for biochemical application. He held the "Millions of Talents Project" of Liaoning province grant in 2015. He has published more than 40 papers in peer-reviewed journals, among which 20 papers were admitted into the periodical source of SCI. He is currently the reviewer of Chemical Engineering Science, Ocean Engineering, etc.

Reference

[1] P. Damborský, J. Švitel, and J. Katrlík. Essays biochem. 2016, *60*, 91

[2] N. Khansili, G. Rattu, and P. M. Krishna. Sens. Act. B 2018, *265*, 35

[3] G. Zanchetta, R. Lanfranco, F. Giavazzi, T. Bellini, and M. Buscaglia, Nanophotonics 2017, *6*, 627

[4] M.C. Estevez, M. Alvarez, and L.M. Lechuga. Laser Photonics Rev. 2012, *6*, 463

[5] C. Chen, X. Hou, and J. Si. IEEE Sens. J. 2018, *18*, 5368

[6] X.Fan, I.M. White, S.I. Shopova, H. Zhu, J.D. Suter, and Y. Sun. Analy chim. acta 2008, *620*, 8

[7] X.X. Jiang, *Doctor Dissertation*, Zhejiang University, December 2015

[8] O. Mitomi, K. Kasaya, and H. Miyazawa. IEEE J. Quant. Electron. 1994, *30*, 1787

[9] I. Day, I. Evans, A. Knights, F. Hopper, S. Roberts, J. Johnston, S. Day, J. Luff, K. Tsang, and M. Asghari. Optical Fiber Communications Conference, Atlanta, Georgia United States, March 2003

[10] S.H. Chen, H. Ma, and X.J. Yi. Acta Optica Sinica 2004, *24*, 756

[11] Sure A, Dillon T, Murakowski J, C. Lin, D. Pustai, and D.W. Prather. Opt. Express 2003, *11*, 3555

[12] J.J. Fijol, E.E. Fike, P.B. Keating, D. Gilbody, J.J. LeBlanc, S.A. Jacobson, W.J. Kessler, and M.B. Frish. The International Society for Optical Engineering, San Jose, CA, United States, May 2003.

[13] G.Z. Masanovic, V.M.N Passaro, and G.T. Reed. IEEE Photon. Tech. Lett. 2003, *15*, 1395

[14] D. Tailaert, R. Baets, and P. Dumon, W.W. Bogaerts, D.V. Thourhout, B. Luyssaert, V. Wiaux, S. Beckx, and J. Wouters. Workshop on Fibers and Optical Passive Components, Palermo, Italy, June 2005

[15] G. Roelkens, T.D. Van, and R. Baets. Opt. Express 2006, *14*, 11622

[16] F.V. Laere, G. Roelkens, M. Ayre, F.V. Laere, G. Roelkens, M. Ayre, J. Schrauwen, and R. Baets. J. Lightwave Technol. 2007, *25*, 151

[17] S.K. Selvaraja, D. Vermeulen, M. Schaekers, E. Sleeckx, W. Bogaerts, G. Roelkens, P. Dumon, D.V. Thourhout , and R. Baets. 2009 Conference on Lasers and Electro-Optics and 2009 Conference on Quantum electronics and Laser Science Conference, Baltimore, MD, USA, June 2009.

[18] A. Foubert, N.V. Beloglazova, M. Hedström, S.D. Saeger. Talanta 2019, *191*, 202

[19] E. Fernandes, P.D. Cabral, R. Campos, J.G. Machado, M.F. Cerqueira, C. Sousa, P.P. Freitas, J. Borme, D.Y. Petrovykh, and P. Alpuim. Appl. surf. sci. 2019, *480*, 709

[20] X.F. Wang, Z. Mei, YY. Wang, and L. Tang. Beilstin J. Nanotech. 2017, *8*, 372

[21] X. Li, Y. Li, Q. Qiu, Q.R. Wen, Q. Zhang, W.J. Yang, L.H. Yuwen, L.X. Weng, and Wang, L.H. J. Colloid Interf. Sci. 2019, *543*, 96

[22] JA Menges, A Clasen, M Jourdain, J Beckmann, C. Hoffmann, J. König, and G. Jung, - Langmuir, 2019, *35*, 2506

[23] S. Prieto-Simin, M. Campas, and J.L Marty. Protein Pept Lett. 2008, *15*, 757

[24] A.K. Yetisen, H. Butt, and S.H. Yun. ACS Sen. 2016, *1*, 493

[25] J.H. Kang, J.H. Moon, S.K. Lee, S.G. Park, S. G. Jang, S. Yang, and S. Yang. Adv. Mater 2008, 20, 3061

[26] S. Pervez, M.A. Nawaz, F. Shahid, A. Aman, I. Tauseef, and S.A.U. Qader. Int. J. Biol. Macromol. 2019, *135*, 1252-1260.

[27] E. Górecka and M. Jastrzębska. Biotechnol. Food Sci. 2011, *75*, 65

[28] N. Miletić and K. Loos. Aust. J. Chem. 2009, *62*, 799

[29] C. Mateo, J.M. Palomo, L.M. van Langen, F. van Rantwijk, and R.A. Sheldon. Biotechnol. Bioeng. 2004, *86*, 273

[30] M. Malmqvist. Nature 1993, *361*, 186

[31] P. Singh. Sens. Act. B 2016, *229*, 110

[32] R.C. Jorgenson and S.S. Yee. Sens. Act. B 1993, *12*, 213

[33] A.P.Vinogradov, A.V. Dorofeenko, , A.A. Pukhov, and A.A. Lisyansky, Phys. Rev. B 2018, *97*, 235407.

[34] A .Yuriy. Opt. Lett. 2018, *43*, 1195

[35] Y. Lee, S.M. Sim, M.R.N. dos Santos, G.D.F. Fernandes, G.O. Cavalcanti, I. Llamas-Garro, and J.M. Kim. 2018 International Conference on Optical MEMS and Nanophotonics (OMN), Lausanne, Switzerland, July 2018.

[36] X.D. Hoa, A.G. Kirk, and M. Tabrizian. Biosens. Bioelectron 2007, *23*, 151

[37] M.A. Wear, M.W.owicki, E.A. Blackburn, I.W. McNae, and M.D. Walkinshaw. FEBS open bio 2017, *7*, 533

[38] E. Pol, H. Roos, F. Markey, F. Elwinger, A. Shaw, and R. Karlsson. Anal. biochem. 2016, *510*, 88

[39] S. Unser, I. Bruzas, , J. He, , and L. Sagle. Sensors 2015, *15*, 15684

[40] Beland P, Krupin O, and Berini P. Biomed Opt Express 2015, *6*, 2908

[41] Y. Zeng, R. Hu, L. Wang, D. Gu, J. He, S.Y. Wu, H.P. Ho, X.J. Li, J.L. Qu, B. Z. Gao and Y. Shao, Nanophotonics 2017, *6*, 1017

[42] A.U. Khan, S. Zhao, and G. Liu. J. Phys. Chem. C. 2016, *120*, 19353

[43] S. Zeng, D. Baillargeat, and H.P. Ho. Chem. Soc. Rev. 2014, *43*, 3426

[44] N.Cathcart, J.I. Chen, and V. Kitaev, Langmuir 2018, *34*, 612

[45] S. Jia, C. Bian, J. Sun, J. Tong, and S. Xia. Biosens. Bioelectron 2018, *114*, 15

[46] K. Hobbs, N. Cathcart, and V. Kitaev. Chem. Comm. 2016, *52*, 9785

[47] X. Liu, Y. Hu, S. Zheng, Y. Liu, Z. He, and F. Luo. Sens. Act. B 2016, *230*, 191

[48] Y. Jia, Y. Peng, J. Bai, X. Zhang, Y. Cui, B. Ning, J. Cui, and Z. Gao. Sens. Act. B 2018, *254*, 629

[49] H. Zhang, Y. Sun, S. Gao, J. Zhang, H. Zhang and D. Song, Small, 2013, *9*, 2537

[50] E. G. Lee, K. M. Park, J. Y. Jeong, S. H. Lee, J. E. Baek, H. W. Lee, J. K. Jung and B.
H. Chung, Anal. Biochem. 2011, *408*, 206

[51] A. H. Severs and R. B. M. Schasfoort. Biosens. Bioelectron.1993, *8*, 365

[52] T. Wink, S. J. van Zuilen, A. Bult and W. P. van Bennekom. Anal. Chem. 1998, *70*, 827

[53]P.K. Jain, W. Huang and M.A. EI-Sayed. Nano Lett 2007, *7*, 2080

[54] S.E. Lee, Q. Chen, R. Bhat, S. Petkiewicz, J.M. Smith, V.E. Ferry, A.L. Correia, A.P. Alicisatos and M.J. Bissell. Nano Lett 2015, *15*, 4564

[55] A. Otto, I. Mrozek, H. Grabhorn, W.J. Akemann. Phys. Condens. Matter 1992, *4*, 1143

[56] J. Su, D. Wang, L. Norbel, J. Shen, Z. Zhao, Y. Dou, T. Peng, J. Shi, S. Mathur, C. Fan, and S. Song. Anal Chem 2017, *89*, 2531

[57] Y. Pang, Z. Rong, J. Wang, R. Xiao, and S. Wang. Biosens. Bioelectron. 2015, *66*, 527

[58] S. Khatua, P.M. Paulo, H. Yuan, A. Gupta, P. Zijlstra, and M. Orrit. ACS Nano 2014, *8*, 4440

[59] H. Sugimoto, S. Yashima, and M. Fujii. ACS Photonics 2018, *5*, 3421

[60]Khan MS and Chaudhair VR. J Fluoresc. 2014, *24*, 751

[61]Cheng ZH, Li G, and Liu MM. Sens. Act. B 2015, *212*, 495

[62] Z. Mei, and L. Tang. Anal. Chem. 2016, *89*, 633

[63] W. Kim, S.H. Lee, Y.J. Ahn, S.H. Lee, J. Ryu, S.K. Choi, and S. Choi. Biosens. Bioelectronics 2018, 111, 59-65.

[64] A. Campu, L. Susu, F. Orzan, D. Maniu, A.M. Craciun, A. Vulpoi, L. Roiban, M. Focsan, and S. Astilean. Front. Chem. 2019, 7, 55.

[65] P. Kozma, F. Kehl, E. Ehrentreich-Förster, C. Stamm, and F.F. Bier. Biosens. Bioelectronics 2014, *58*, 287

[66] C. Chen, X. Hou, and J. Si. Nanotechnology 2019, *30*, 1

[67] F. Dell'Olio, and V.M. Passaro. Opt. Express 2007, *15*, 4977.

[68] R.F. Oulton, V.J. Sorger, D.A. Genov, D.F.P. Pile, and Zhang, X. Nat. Photonics 2008, *2*,496

[69] C.A. Barrios, K.B. Gylfason, B. Sanchez, A. Griol, H. Sohlström, M. Holgado, and R. Casquel. Opt. Lett. 2007, *32*, 3080

[70] K.B. Gylfason, C.F. Carlborg, A. Kaźmierczak, F. Dortu, H. Sohlström, L. Vivien, C.A. Barrios, W. Wijngaart and G. Stemme. Opt. Express 2010, *18*, 3226-3237.

[71] Khodadaa I, Clarke N, Khorasaninejad M, D. Henneke, and S.S. Saini. Appl. Opt. 2014, *53*, 5169

[72] C. Pan and B.M.A. Rahman. IEEE J. Sel. Topics Quantum Electron. 2017, *23*, 4400108

[73] X. Sun, D. Dai, L. Thylen and L. Wosinski. Opt. Express 2015, *23*, 25688

[74] A.D. Falco, L. Ofaolain, and T.F. Krauss. Appl. Phys. Lett. 2008, *92*, 083501

[75] A.D. Falco, L. Ofaolain, and T.F. Krauss. Appl. Phys. Lett. 2009, *94*, 063503

[76] K. Misiakos, I. Raptis, A. Salapatas, E. Makarona, A.otsialas, M. Hoekman, R. Stoffer and G. Jobst. Opt. Express 2014, *22*, 8856

[77] R.G. Heideman, R.P.H.Kooyman, and J. Greve. Sens. Act. B 1991, *4*, 297

[78] J. Ingenhoff, B. Drapp, and G. Gauglitz. J Anal Chem 1993, *346*, 580

[79] B. Prieto, B. Sepulveda, A. Calle, F. Prieto, B. Sepúlveda, A. Llobera, C. Domínguez, A. Abad, A. Montoya and L.M. Lechuga, Nanotechnology 2003, *14*, 907

[80] A. Psarouli, A. Salapatas, A. Botsialas, P.S. Petrou, I. Raptis, E. Makarona, G. Jobst, K. Tukkiniemi, M. Sopanen, R. Stoffer, S.E. Kakabakos and K. Misiakos. Sci Rep 2015, *5*, 17600

[81] K. Gajos, M. Angelopoulou, P. Petrou, K. Awsiuk, S. Kakabakos, W. Haasnoot, A. Bernasik, J. Rysz, M.M. Marzec, K. Misiakos, I. Raptis and A. Budkowski. Applied Surface Science, 385, 529-542. Appl Surf Sci 2016, *385*, 529

[82] K. Gajos, A. Budkowski, P. Petrou, V. Pagkali, K. Awsiuk, J. Rysz, A. Bernasik, K. Misiakos, I. Raptis and S. Kakabakos. Appl Surf Sci 2018, *444*, 187

[83] N.F. Hartman, J.C. Wyvill, D.P. Campebell and P. Edmonds. Proc. SPIE 1995, *2345*, 128

[84] B.H. Schneider, J.G. Edwards, and N.F..Hartman. Clin. Chem. 1997, *43*, 1757

[85] B.H. Schneider, E.L. Dickinson, M.D. Vach, J.V. Hoijer, and L.V. Howard. Biosens Bioelectron 2000, *15*, 13

[86] J. Escorihuela, M.A. Gonzalez-Martinez, J.L. Lopez-Paz, R. Puchades, A. Maquieira, and D. Gimenez-Romero. Chem. Rev. 2015, *115*, 265

[87] M.M. Ouberai, K. Xu，and M.E. Welland. Biomaterials 2014, *35*, 6157

[88] F. Huang, P. Xu, and H. Liang. Biosens. Bioelectron 2014, *51*, 317

[89] A. Brandenburg, R. Krauter, C. Kunzel, M. Stefan, and H. Schulte. Appl. Opt. 2000, *39*, 6396

[90] A. Ymeti, J.S. Kanger, J. Greve, G.A.J. Besselink, P.V. Lambeck, R. Wijn, and R.G. Heideman. Biosens Bioelectron. 2005, *20*, 1417

[91] K. Schmitt, B. Schirmer, and A. Brandenburg. Proc. SPIE 2005, *5855*, 459

[92] K. Schmitt, B. Schirmer, C. Hoffmann, A. Brandenburg, and P. Meyrueis. Biosens Bioelectron. 2007, *22*, 2591

[93] G.C. Righini, and S. Soria. Sensors 2016,*16*, 905

[94] K.J. Vahala. Nature 2003, *424*, 839

[95] M.R. Foreman, J.D. Swaim, and F. Vollmer. Adv. Opt. Photonics 2015, *7*, 168

[96] A. Bozzola, S. Perotto, and F. Angelis. Analyst 2017, *142*, 883

[97] F. Dell'Olio, D. Conteduca, C. Ciminelli and M.N. Armenise. Opt. Express 2015, 23 28593

[98] X. Tu, S.L. Chen, C. Song, T. Huang, and L.J. Guo. IEEE Photonics J. 2019, 11, 1

[99] J. Yu, E. Lewis, G. Brambilla, and P. Wang. Sensors 2018, 18, 2515.

[100] H. Wan, J. Chen, C. Wan, Q. Zhou, J. Wang, and Z. Zhang. Biomed. Opt. Express 2019, 10, 3929

[101] Z. Guo, Q. Lu, C. Zhu, B. Wang, Y. Zhou, and X. Wu. Opt. Express 2019, 27, 12424-12435.

[102] A.K. Mallik, G. Farrell, M. Ramakrishnan, V. Kavungal, D. Liu, Q. Wu, and Y. Semenova. Opt. express 2018, 26, 31829

[103] M.D. Baaske, M.R. Foreman and F. Vollmer. Nat. Nanotechnol., 2014, 9, 933

[104] D.K. Armani, T.J. Kippenberg, S.M. Spillane and K.J. Vahala. Nature 2003, 421, 925

[105] D. Farnesi, F. Chiavaioli, G.C. Righini, S. Soria, C. Trono, P. Jorge, and G.N Conti. Opt. Let. 2014, *39*,6525

[106] A.B. Petermann, A. Varkentin, B. Roth, U. Morgner, and M. Meinhardt-Wollweber. Opt. Express, 2016, *24*, 6052

[107] J.M..Ward, N. Dhasmana, and S.N. Chormaic. Eur Phys J-Spec Top 2014, *223*, 1917

[108] V. Zamora, A. Díez, M.V. Andrés, and B. Gimeno. Photonic Nanostruct. 2011, *9*, 149

[109] G. Gaur, S. Hu, R.L. Mernaugh, I.I. Kravchenko, S.T., Retterer, and S.M. Weiss. Sens. Act. B 2018, *275*, 394

[110] J.K. Poon. Nat. Photonics 2018, *12*, 255.

[111] Z. Su, N. Li, H.C. Frankis, E.S. Magden, T.N. Adam, G. Leake, D. Coolbaugh, J.D.B. Bradley, and M.R. Watts. Opti. Express 2018, *26*, 11161

[112] A.V. Shneidman, K.P. Becker, M.A. Lukas, N. Torgerson, C. Wang, O. Reshef, M.J. Burek, K. Paul, J.M. McLellan, and M. Lončar, Acs Photonics 2018, *5*, 1839

[113] F. Angelis, M. Patrini, M. Das, I. Maksymov, M. Galli, L. Businaro, L.C. Andreani, M. Enzo and E. Fabrizio. Nano Lett.2008, *8*, 2321

[114] V.R. Dantham, S. Holler, C. Barbre, D. Keng, V. Kolchenko and S. Arnold. Nano Lett. 2013, *13*, 3347.

[115] M. Zhang, G. Wu, and D. Chen. Appl. Opt. 2015, *54*, 7131

[116] D. Urbonas, A. Balcytis, M. Gabalis, K. Vaskevicius, G. Naujokaite, S. Juodkazis and R. Petruskevicius. Opt. Lett. 2015, *40*, 2977

[117] L. Zhou, X. Sun, X. Li and J. Chen. Sensors 2011, *11*, 6856

[118] H. Nadgaran and M.A. Garaei. J. Appl. Phys. 2015, *118*, 043101

[119] E.L. Runnerstrom, A. Bergerud, A. Agrawal, R.W. Johns, C.J. Dahlman, A. Singh, S.M. Selbach, and D.J. Milliron. Nano Lett. 2016, *16*, 3390

[120] E. Yablonovitch. Phys. Rev. Lett. 1987, *58*, 2059

[121] S. John. Phys. Rev. Lett. 1987, *58*, 2486

[122] J. Hou, M. Li, and Y. Song. Sci Sin Chim. 2016, *46*, 1080

[123] S.G. Johnson, A. Mekis, S. Fan, and J.D. Joannopoulos. Comput. Sci. Eng., 2001, 3, 38

[124] S. Robinson, and N. Dhanlaksmi. Photonic Sens. 2017, *7*, 11

[125] H. Shafiee, E.A. Lidstone, M. Jahangir, F. Inci, E. Hanhauser, T.J. Henrich, D.R. Kuritzkes, B.T. Cunningham, and U. Demirci. Sci. Rep. 2014, *4*, 4116

[126] Y. Tan, J.F. Halsey, T. Tang, S.V. Wetering, E. Taine, M.V. Cleve, and B.T. Cunningham. Biosens Bioelectron 2016, *77*, 194

[127] A.A. Rifat, G.A. Mahdiraji, R. Ahmed, D.M. Chow, Y.M. Sua, Y.G. Shee, and F.M. Adikan. IEEE Photonics J. 2015, *8*, 1

[128] R.D. Peterson, W. Chen, B.T. Cunningham, and J.E. Andrade. Biosens. Bioelectron. 2015, *74*, 815

[129] S.M. Lo, S. Hu, G. Gaur, Y. Kostoulas, S.M. Weiss, and P.M. Fauchet. Opt. Express 2017, *25*, 7046

[130] M.S. Mohamed, M.F.O. Hameed, N.F. Areed, M.M. El-Okr, and S.S.A. Obayya, Appl. Comput. Electrom. 2016, *31*, 836

[131] S. Pal, A.R. Yadav, M.A. Lifson, J.E. Baker, P.M. Fauchet, and B.L. Miller. Biosens. Bioelectron. 2013, *44*, 229

[132] A.E. Cetin, and S.N. Topkaya. Biosens. Bioelectron. 2019, *132*, 196

[133] R. Arunkumar, T. Suaganya, and S. Robinson, Photonic Sens. 2019, *9*, 69

[134] S. Arafa, M. Bouchemat, T. Bouchemat, A. Benmerkhi, and A. Hocini. Opt. Commun. 2017, *384*, 93

[135] E. Choi, Y. Choi, Y.H.P. Nejad, K. Shin, and J. Park. Sens. Act. B 2013, *180*, 107

[136] H. Inan, M. Poyraz, F. Inci, M.A. Lifson, M. Baday, B.T. Cunningham, and U. Demirci, Chem Soc Rev. 2017, *46*, 366

[137] C.J. Choi and B.T. Cunningham. Lab Chip 2007, *7*, 550

[138] M. Scullion, T. Krauss, and A. Di Falco. Sensors 2013, *13*, 3675

[139] D. Zhang and Q. Liu. Biosens Bioelectron. 2016, *75*, 273

[140] D. Gallegos, K.D. Long, H. Yu, P.P. Clark, Y. Lin, S. George, P. Nath, and B.T. Cunningham. Lab Chip 2013, *13*, 2124

[141] N. Lee, C. Wang, and J. Park. RSC advances 2018, *8*, 22991

[142] E. Mastronardi, A. Foster, X. Zhang, M.C. DeRosa. Sensor 2014,*14*, 3156

[143] R. Verma, R.R. Adhikary, R. Banerjee. Lab Chip. 2016, *16*, 1978

[144] Z. Cai, L.A. Luck, D. Punihaole, J.D. Madura, and S.A. Asher. Chem. Sci. 2016, *7*, 4557

[145] B. Maeng, Y. Park, and J. Park. RSC Advances 2016, *6*, 7384

[146] J. Ren, H. Xuan, C. Liu, C. Yao, Y. Zhu, X. Liu, and L. Ge, RSC Advances 2015, *5*, 77211

[147] X. Xu, H. Subbaraman, S. Chakravarty, A. Hosseini, J. Covey, Y. Yu, D. Kwong, Y. Zhang, W.C. Lai, Y. Zou, N. Lu, and R. T. Chen. ACS Nano. 2014, *8*, 12265

[148] X. Zhang, G. Chen, F. Bian, L. Cai, and Y. Zhao. Adv. Mater. 2019, 1902825.

[149] B. Lee. Opt. Fiber Technol. 2003, *9*, 57

[150] S.K. Shukla, C.S. Kushwaha, T. Guner, M.M. Demir. Opt. Pt. Laser Technol. 2019, *115*, 404

[151] H.E. Joe, H. Yun, S.H. Jo, M.B.G. Jun, B.K. Min. Int. J. Pr. Eng. Man.-GT. 2018, *5*, 173

[152] J. Li, K. Liao, X. Kong, S. Li, X. Zhang, X. Zhao, and C. Sun. Appl. Sci-Basel

2017, *7*, 419.

[153] X. Qiao, Z. Shao, W. Bao, and Q. Rong. Sensors 2017, *17*, 429

[154] S. Hong, W. Jung, T. Nazari, S. Song, T. Kim, C. Quan, and K. Oh. Opt. letters 2017, *42*, 1943

[155] J. Huang, D.T. Pham, C. Ji, Z. Wang, and Z. Zhou. Measurement 2019, *134*, 226

[156] C. Teng, H. Deng, H. Liu, H.Yang, L.Yuan, J. Zheng, and S. Deng. Photonics 2019, *6*, 40

[157] Y.M. Kamil, M.A. Bakar, M.A. Mustapa, M.H. Yaacob, N.H.Z. Abidin, A. Syahir, H.J. Lee, and Mahdi, M.A. Sens. Act. B 2018, *257*, 820

[158] S. Korposh, S.W. James, S.W. Lee, and R.P. Tatam. Sensors 2019, *19*, 2294.

[159] S.S.Chong, A.A.A. Raman, S.W. Harun, and H. Arof. IEEE Sens. J. 2015, *15*, 3903

[160] M.I. Zibaii, H. Latifi, A. Asadollahi, A.H. Bayat, L. Dargahi, and A. Haghparast. J. Lightwave Technol. 2016, *34*, 4516

[161] M. Arjmand, H. Saghafifar, M. Alijanianzadeh, and M. Soltanolkotabi. Sens. Act. B 2017, *249*, 523

[162] H.Y. Tam, S.Y. Liu, B.O. Guan, W.H. Chung, T.H. Chan, and L.K. Cheng. Advanced Sensor Systems and Applications II. International Society for Optics and Photonics 2005, *5634*, 85.

[163] C.L. Wei, C.C. Lai, S.Y. Liu, W.H. Chung, T.K. Ho, H.Y. Tam, S.L. Ho, A. McCusker, J. Kam, and K.Y. Lee. IEEE Sens. J. 2010, *10*, 1905

[164] J. Xu, D. Yang, C. Qin, Y. Jiang, L. Sheng, X. Jia, Y. Bai, X. Shen, H. Wang, X. Deng, L. Xu and S. Jiang. Sensors 2015, *15*, 29648

[165] T. Sun, H. Fang, W. Liu, and Y. Ye. Agr. Forest Meteorol. 2017, *233*, 143

[166] V. Bense, TRead, and A. Verhoef. Agr. Forest Meteorol. 2016, *220*, 207.

[167] R. Correia, S. James, S.W. Lee, S.P. Morgan, S. Korposh, and S.W. Lee. J. Opt. 2018, *20*, 073003

[168] D. Polito, M.A. Caponero, A. Polimadei, P. Saccomandi, C. Massaroni, S. Silvestri and E.J. Schena. Med. Device 2015, *9*,041006

[169] L. Xiong, G. Jiang, Y. Guo, and H. Liu. IEEE Sens. J. 2018, *18*, 3632

[170 C. Campanella, A. Cuccovillo, C. Campanella, A. Yurt, and V. Passaro. Sensors 2018, *18*, 3115

[171] A. Arora, M. Esmaeelpour, M. Bernier, and M.J. Digonnet. Opt. Lett. 2018, *43*, 3337

[172] A. Asseh, S. Sandgren, H. Ahlfeldt, B. Sahlgren, R. Stubbe, G. Edwall, Fiber Integrated Opt. 1998, *17*, 51

[173] A. Iadicicco, A. Cusano, S. Campopiano, A. Cutolo, M. Giordano. IEEE Sens. J. 2005, *5*, 1288

[174] A.N. Chryssis, S.S. Saini, S.M. Lee, H. Yi, W.E.entley, M. Dagenais. IEEE J. Sel. Top. Quant. 2005, *11*, 864

[175] M. Lei, Y.N. Zhang, B. Han, Q. Zhao, A. Zhang, and D. Fu. IEEE Sens. J. 2018, *18*, 7499

[176] A. Zrelli, M. Bouyahi, and T. Ezzedine. Optik 2016, *127*, 7326

[177] G. Pereira, M. McGugan, and L.P. Mikkelsen. Polym. Test. 2016, *50*, 125

[178] R. Oliveira, J.H. Osório, S. Aristilde, L. Bilro, R.N. Nogueira, and C.M. Cordeiro. Meas. Sci. Technol. 2016, *27*, 075107

[179]Y. Chen, Q. Han, T. Liu, F. Liu, Y. Yao. IEEE Sens. J. 2015, *15*, 6432

[180] C. Li, T. Ning, J. Li, L. Pei, C. Zhang, C. Zhang, H. Li., and X. Wen. Opt. Laser Technol. 2017, *90*, 179

[181] Y. Dong, S. Xiao, B. Wu, H. Xiao, and S. Jian. IEEE Sens. J. 2019, *19*, 1362

[182] J.F. Masson. ACS sensors 2017, *2*, 16

[183] K. Mahato, P.K. Maurya, and P. Chandra. 3 Biotech 2018, *8*, 149.

[184] F. Ejeian, P. Etedali, H.A. Mansouri-Tehrani, A. Soozanipour, Z.X. Low, M. Asadnia, A. Taheri-Kafrani and A. Razmjou. Biosens. Bioelectron 2018, *118*, 66

[185] N. Khansili, G. Rattu, and P.M. Krishna. Sens. Act. B 2018, *265*, 35

[186] T. Kaminski, A. Gunnarsson, and S. Geschwindner. ACS sensors 2016, *2*, 10

[187] P. Rivero, J. Goicoechea, and F. Arregui. Polymers 2018, *10*, 280.

[188] C. Chen, X. Hou, and J. Si. Opt.Express 2017, *25*, 31294

[189] C. Chen, X. Hou, and J. Si. Nanotechnol. Rev. 2018, *7*, 11

[190] F. Esposito, L. Sansone, C. Taddei, S. Campopiano, M. Giordano, and A. Iadicicco. Sens. Act. B 2018, *274*, 517

[191] R.Kant, and B.D. Gupta. J. Lightwave Technol. 2018, *36*, 4018

[192] M.S. Rahman, M.R. Hasan, K.A. Rikta, and M.S. Anower. Opt. Mater. 2018, *75*, 567